## 2. GLOBAL CLIMATE—A. Horvitz, Ed.

### a. *Overview*—A. Horvitz

The year 2007 was notable for pronounced warmth at the surface and throughout the troposphere. The global land and ocean combined surface temperature ranked within the 10 highest on record, while the average land temperature was the warmest since records began in 1880, with an annual departure of +0.64°C. The annual global mean temperature in the low to midtroposphere was among the five warmest since records began in 1958, about 0.2°C cooler than the warmest year of 1998.

For the fourth consecutive year, the annual precipitation averaged over global land surfaces was above the 1961–90 base period mean, with a wet anomaly of approximately 8 mm (0.7%) in 2007. Over the tropical Pacific, the 2006 El Niño ended abruptly in February 2007. During the second half of the year negative SST anomalies expanded westward from the equatorial eastern Pacific as a moderate-to-strong La Niña episode developed by year's end.

The 12-month running mean of Northern Hemisphere snow cover extent was below the long-term average throughout the year. The negative 12-month anomaly at year's end had not occurred since the record lows of the satellite era were observed between 1988 and 1990. The Arctic and the Amazon basin and its environs both exhibited strong deviations in total cloud cover in 2007, which may have resulted from changes in atmospheric moisture and surface temperatures (for the Arctic) and land use change (for the Amazon).

The globally averaged concentration of $CO_2$ continued to increase in 2007, rising to 382.7 ppm, an increase of 1.6 ppm over the 2006 global mean value. $CH_4$ and CO concentrations were also higher in 2007, with the preliminary global averages increasing to 1,782.2 ppb and 84 ppb, respectively. The global mean mixing ratios at the end of 2007 for $N_2O$ was 321.4 ppb while $SF_6$ was 6.29 ppt, an increase of 1.4 ppb and 0.29 ppt, respectively, over 2006. Additionally, HCFCs continued to increase and by mid-2007 chlorine accounted for by the three most abundant HCFCs amounted to 237 ppt, or 8.8% of all chlorine carried by long-lived halocarbons of anthropogenic chlorine (not including Cl from $CH_3Cl$).

The 2006 elevated aerosol levels seen at the far northern latitudes or around Indonesia were absent in 2007, and smoke from biomass burning over the Amazon basin, an indication of regional deforestation, exhibited levels that were inline with the increasing aerosol trend observed from 2000 through 2005. Over the Southern Ocean, long bands of greater wind speeds in March through August suggested an atypically strong surface manifestation of the polar vortex during the austral winter. This chapter concludes with a discussion of teleconnection patterns including the mean December–February 2006–07 500-hPa circulation pattern, which was characterized by a large degree of zonal symmetry that projected strongly onto the Arctic Oscillation.

### b. *Global temperature*

#### 1) Surface temperature—M. J. Menne

The global average surface temperature in 2007 was among the 10 warmest years on record. As shown in Fig. 2.1, the 2007 annual average temperature ranked from second to eighth highest on record based on three global datasets maintained independently by NOAA's NCDC (fifth highest), NASA's GISS (second highest), and the University of East Anglia–CRU/UKMO (eighth highest). Calculated as a linear trend, the rates of temperature change are 0.065°, 0.066°, and 0.074°C decade$^{-1}$ since 1901 for the NOAA, NASA, and CRU/UKMO analyses, respectively. However, as Fig. 2.1 shows, the change in global temperature has been nonlinear, with the rise from 1979 to 2007 nearly 3 times greater than the century-scale trend. In addition, the pattern of warming has not been uniform, as shown in Fig. 2.2.

All three global temperature analyses shown in Fig. 2.1 are based on air temperature data over land and SST derived from ship reports, buoys, and satellite observations. The NOAA surface temperature analysis is described in Smith and Reynolds (2005), the NASA analysis is described in Hansen et al. (2001), and the CRU/UKMO analysis (HadCRUT3) is described in Brohan et al. (2006). Because the three groups use different reconstruction and interpola-

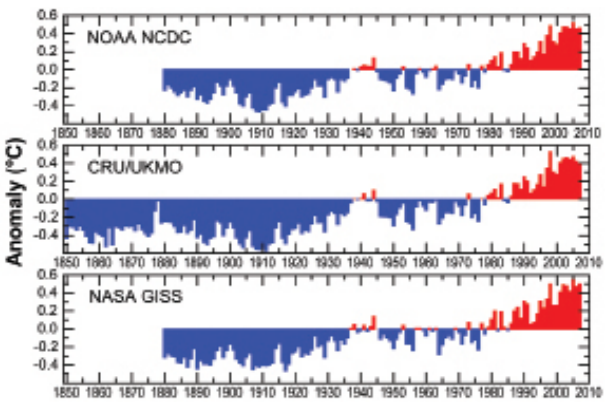


**Fig. 2.1. Annual global surface temperature departures from the 1961 to 1990 average. [Sources: NOAA/NCDC; CRU/UKMO (HadCRUT3); and NASA GISS.]**

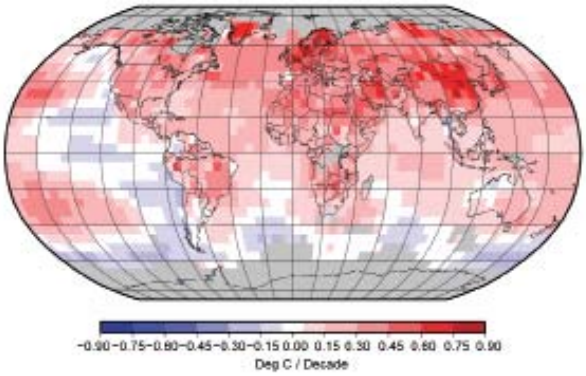


**Fig. 2.2. Pattern of linear temperature trends for the period 1979 to 2007. Gray areas indicate data-sparse regions. [Source: NOAA/NCDC.]**

tion approaches, the analyses differ most in regions with sparse data. In terms of the global averages, and where observations are plentiful, the three surface temperature reconstructions are in good agreement. The differences in annual rankings in recent years are caused in part by how the different groups treat data sparse regions. For example, the NASA analysis expands estimates of temperature anomalies across the Arctic where values were at or near record levels in 2007. Despite these differences, the uncertainty in the calculations implies that the value for 2007 in all three datasets is effectively indistinguishable from values in several of the other high ranking years. The addition of error bars to the NCDC global surface temperature time series (Fig. 2.3a) illustrates the uncertainty in calculations of annual global temperature rankings.

Warming has occurred in both land and sea surface temperatures. As might be expected given the tremendous thermal capacity of the oceans, land temperatures have risen at over twice the rate of the ocean surface since 1979 (about 0.30° versus 0.12°C decade$^{-1}$). Worldwide, land surface temperatures in 2007 ranked as highest on record according to the NOAA record while SSTs ranked as ninth highest (Fig. 2.4b). (A preliminary analysis of the influence of SSTs on land surface temperatures in 2007 is provided in the adjoining sidebar discussion.) The top 10 ranking for SSTs is noteworthy because it occurred at a time when the equatorial Pacific Ocean was in the cool phase of the El Niño–La Niña cycle. The geographic distribution of the 2007 annual temperature anomalies is shown in Fig. 2.4 (see chapter 6 for additional details of regional temperatures in 2007).

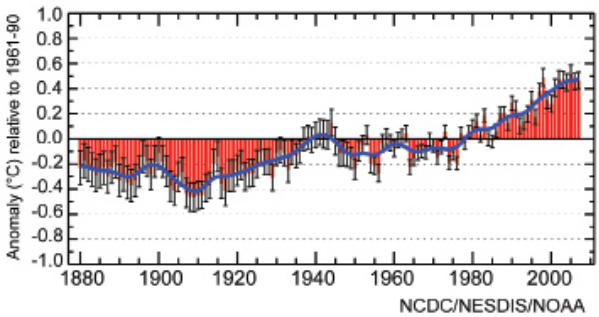


**Fig. 2.3a. Annual global surface temperature departures (red bars) from the 1901 to 2000 average with error estimates (black lines). [Source: NOAA/NCDC (Smith and Reynolds 2005).]**

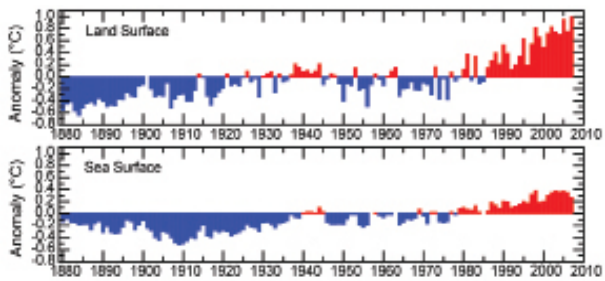


**Fig. 2.3b. Global land and sea surface temperature anomalies with respect to the 1961 to 1990 average. [Source: NOAA/NCDC.]**

2) Upper-air temperatures—J. R. Christy

The temperature variations of three broad atmospheric layers, the LT to MT (Sfc–300 hPa), the MT to LS (Sfc–70 hPa), and the upper troposphere to LS (150–20 hPa) are monitored by two observing systems, radiosondes, and satellites. Three radiosonde-based products are available, HadAT2 (Thorne et al. 2005) based on about 650 stations, RATPAC (Free et al. 2005) based on 85 stations, and RAOBCORE based on about 1,100 stations (Haimberger 2007).

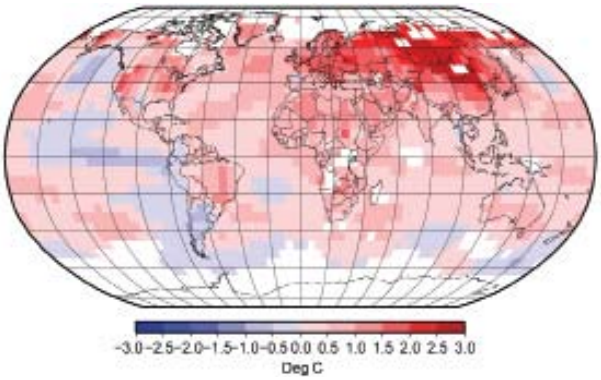


**Fig. 2.4. Geographic distribution of temperature anomalies in 2007. Departure from the 1961 to 1990 average. [Source: NOAA/NCDC.]**

Satellite products are the latest versions updated from last year, LT, MT, and LS from the UAH (Christy et al. 2003; Spencer et al. 2006; v5.2 LT, v5.1 MT, and LS) and RSS (Mears et al. 2003; Mears and Wentz 2005; v3.1 LT, v3.0 MT, and LS). Here "annual" is defined as December to November, otherwise known as the meteorological year.

The annual, global mean LT anomaly for 2007 was second to fifth warmest (for reference: HadAT2:2nd, RATPAC:4th, RAOBCORE:2nd, UAH:4th, RSS:5th) among the datasets since records began (1958 for radiosondes or 1979 for the satellite record, Fig. 2.5). On average, this was about 0.2°C cooler than the warmest year 1998. Some datasets also ranked the NH anomaly as second warmest following 1998. All datasets are consistent with global trend values of +0.16 ± 0.03°C decade$^{-1}$ since 1979 and +0.16 ±0.02°C decade$^{-1}$ since 1958 (Fig. 2.5; Table 2.1).

Regionally, the tropical LT values began the year warmer than the 1979–98 average during a minor El Niño while the global LT temperature in January was the warmest monthly anomaly since the 1998 El Niño in some datasets. By the end of the year, however, a developing and substantial La Niña dropped tropical temperatures below average. The north polar regions continued to be above average with trends since 1979 above +0.4°C decade$^{-1}$ while the south polar regions were near the long-term average.

A similar picture is indicated for the MT layer (not shown), which includes some stratospheric influence. The rankings for 2007 placed this layer from third to sixth warmest (for reference: HadAT2:3rd, RATPAC:6th, RAOBCORE:3rd, UAH:5th, RSS:5th) depending on the datasets. Linear trends are more negative than LT due to the influence of the cooling stratosphere (Table 2.1).

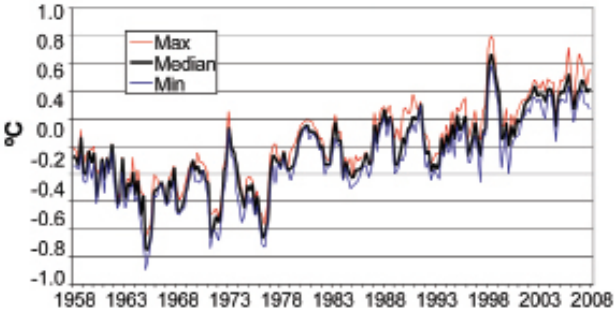


**Fig. 2.5. Time series of seasonal anomalies of the lower troposphere, LT, as the median of the various datasets, with respect to 1979–88 (black). The red and blue lines represent the highest and lowest values, respectively, reported by any of the sources.**

The quasi-biennial oscillation shifted to the easterly or cold phase in 2007 and thus tropical stratospheric temperatures (LS) in the latter half of 2007 were cooler than the similar period in 2006 by about 1.2°C. Globally, among the datasets, the 2007 annual anomaly ranked from the second to sixth coldest (for reference: HadAT2:2nd, RATPAC:2nd, RAOBCORE:6th, UAH:2nd, RSS:3nd). As has been

**Table 2.1. Linear trends (°C decade$^{-1}$) of global and tropical (20°S–20°N) anomalies for 1958–2007. In parentheses are trends for 1979–2007.**

| | HadAT2* | RATPAC* | RAOBCORE* | UAH** | RSS** |
|---|---|---|---|---|---|
| Global LT | +0.16 (+0.18) | +0.16 (+0.17) | +0.14 (+0.17) | (+0.14) | (+0.18) |
| Tropical LT | +0.12 (+0.09) | +0.14 (+0.13) | +0.13 (+0.12) | (+0.08) | (+0.18) |
| Global MT | +0.09 (+0.07) | +0.08 (+0.05) | +0.10 (+0.12) | (+0.06) | (+0.12) |
| Tropical MT | +0.09 (+0.02) | +0.08 (+0.03) | +0.12 (+0.12) | (+0.05) | (+0.15) |
| Global LS | –0.36 (–0.53) | –0.39 (–0.62) | –0.30 (–0.39) | (–0.43) | (–0.31) |
| Tropical LS | –0.34 (–0.54) | –0.44 (–0.65) | –0.25 (–0.34) | (–0.38) | (–0.31) |

* Radiosonde datasets are characterized by more limited coverage with few data south of 50°S latitude and little in oceanic areas.

**UAH coverage is 85°S to 85°N, RSS 70°S to 85°N. Since less warming has been observed in the high southern latitudes, their inclusion tends to reduce "global" trends, e.g., the UAH global LT trend is 0.02°C decade$^{-1}$ more positive when excluding latitudes south of 50°S.

## THE INFLUENCE OF SSTs ON GLOBAL LAND SURFACE TEMPERATURES—M. P. HOERLING IN CONJUNCTION WITH THE NOAA CSI TEAM

Globally averaged land temperatures for 2007 were the warmest since records began in 1880, with a mean annual departure of +0.64°C above the 1971–2000 average based on the CRU/UKMO analysis. Land temperatures were anomalously warm almost everywhere over the globe (Fig. 2.6, top panel).

The connection between the record global land temperatures of 2007 and global SST conditions was investigated with three AGCM simulations forced with the monthly evolution of observed SSTs (so-called AMIP experiments; Gates 1992). For each AGCM, an ensemble of 50 realizations was made without the effects of radiative forcing due to changes in atmospheric chemical composition. The multimodel ensemble averaged land surface temperature response in 2007 is warm at virtually all locations (Fig. 2.6, middle panel), with a mean annual globally averaged land temperature departure of +0.26°C computed with respect to the 1971–2000 climatological mean. The PDF of simulated globally averaged 2007 land surface temperature departures for each of the 150 AMIP runs is shown in Fig. 2.7 (left panel), along with the PDF of 150 members of the control runs that used 1971–2000 climatological SSTs. The PDF indicates that 1) a majority of simulations for 2007 had a positive land surface temperature anomaly and 2) while SSTs in 2007 greatly elevated the chances that global land surface temperatures would be above normal, no single run generated a departure as large as observed. This SST-only-forced analysis suggests that the SST-forced response, although of the same sign as the 2007 observed record land temperatures, was not the leading cause.

The relationship between the record global land temperature of 2007 and GHG forcing was investigated using the coupled model simulations that were used in the IPCC Fourth Assessment Report.

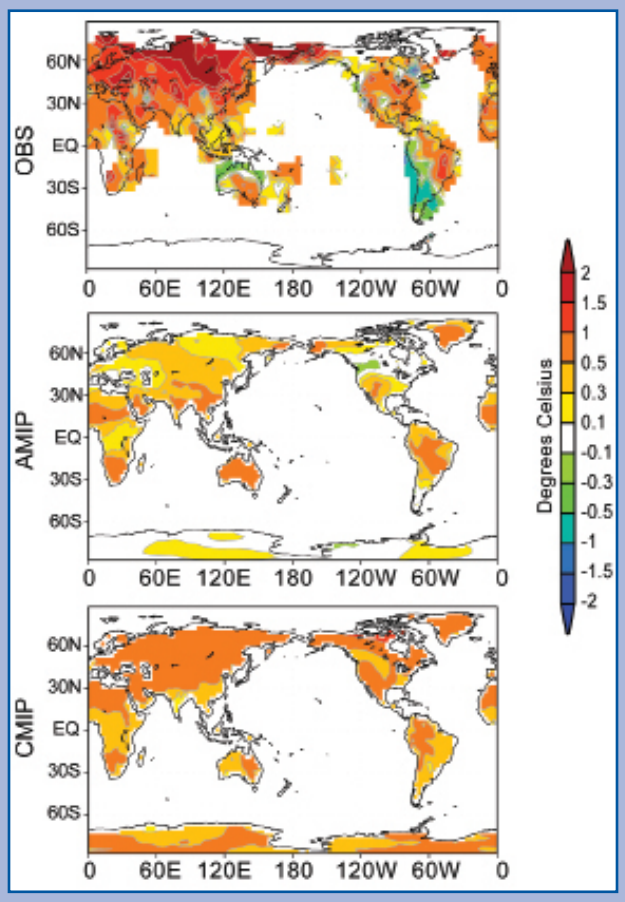


**Fig. 2.6. (top) Observed and simulated 2007 annually averaged land surface temperature departure based on (middle) AMIP ensemble and (bottom) CMIP ensemble experiments. Reference is 1971–2000 climatologies. AMIP refers to atmospheric climate models forced with the monthly varying observed 2007 global sea surface temperatures. CMIP refers to coupled ocean–atmosphere climate models forced with estimated 2007 greenhouse gas concentrations. See text for details on model runs. [Source: NOAA CSI Team.]**

the case for most of the last few years, there was not a dramatic cooling of the south polar region in the austral spring. Even so, all datasets indicate significant cooling over the period on a global basis (Table 2.1), though since about 1995, the global trends have not been remarkable (Fig. 2.8).

### c. *Hydrologic cycle*

#### 1) Global precipitation

##### *(i) Over land*—D. H. Levinson and J. H. Lawrimore

The focus of this section is on land-based precipitation and the spatiotemporal variations observed in 2007 using in situ gauge data from the GHCN dataset (Peterson and Vose 1997). The annual and seasonal

This "CMIP archive" of model data (which included 22 coupled atmosphere–ocean models and a total ensemble size of 48 simulations for 2007) used projected GHG concentrations based on a business-as-usual scenario (A1B) extended from the historical climate of the twentieth century runs that ended in 1999. The 2007 land surface temperature anomalies averaged across all 48 model simulations are shown in Fig. 2.7 (right panel). Warm surface temperature departures (relative to the CMIP model climatologies of 1971–2000) occur over all land points, with a mean annual globally average land temperature departure of +0.40°C. The PDF of simulated globally averaged land surface temperature departures for each of the 48 runs is shown in Fig. 2.7 (right panel), along with the distribution of all CMIP simulated global land surface temperatures during the reference period of 1971–2000 (comprising 1,440 samples; 30 yr × 48 runs). The PDF indicates that 1) almost all simulations for 2007 had a positive land surface temperature anomaly and 2) 2007 GHG forcing greatly elevated the chances that global land surface temperatures would be above normal, with a few runs generating 2007 departures larger than the record observed warmth. The magnitude of the land surface warmth is appreciably greater in the CMIP ensemble than in the AMIP ensemble, suggesting that GHG forcing was a leading cause for the 2007 record land temperatures.

In conclusion, the analysis indicates that greenhouse gas forcing was a likely attributing factor raising global mean land temperatures in 2007. That signal (defined as the multimodel mean response) alone, however, cannot explain the record warmth that was observed. Further, the increase of GHG forcing in 2007 led to a 100-fold increase in the probability of land temperatures exceeding the 2007 observed +0.64°C record (from a less than 0.1% chance for 1971–2000 GHG forcing to a 10% probability under the 2007 GHG forcing scenario). At least one pathway by which GHG forcing raised land temperature was via their influence on the observed SSTs, although as judged from the AMIP simulations this alone cannot explain the record warmth.

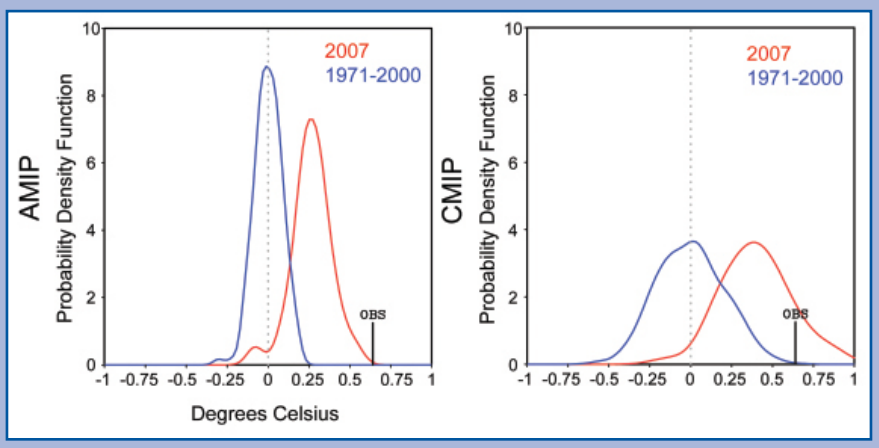


**Fig. 2.7. PDFs of the simulated globally averaged 2007 (red) annual land surface temperatures based on (left) individual 150 AMIP runs and (right) the individual 48 CMIP runs. The PDFs of simulated globally averaged annual land surface temperatures during the reference period of 1971–2000 are shown as the blue PDF curves. The observed globally averaged 2007 annual land surface temperature departure of +0.64°C is plotted by the vertical tic mark. [Source: NOAA CSI Team.]**

departures covering the period 1901 to 2007 were analyzed, and precipitation anomalies determined with respect to the 1961–90 mean for those stations with a minimum of 25 yr of data during the 30-yr base period (Vose et al. 1992). In addition, highlights of selected regional precipitation anomalies are also included below (see chapter 6 for more complete details of regional precipitation patterns and variability).

In 2007, the annual precipitation averaged over all global land surfaces was approximately 8 mm (0.7%) above the 1961–90 base period mean (Fig. 2.9a). It was the fourth consecutive year with above average global precipitation, although the anomaly was sig-

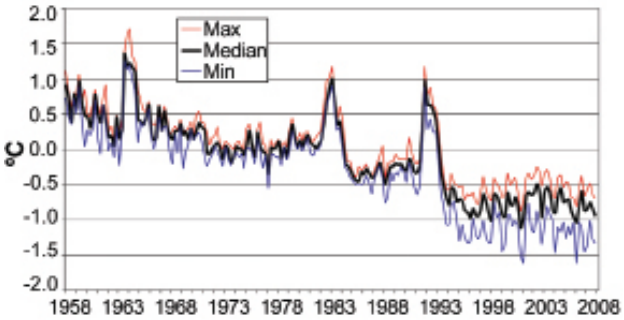


**Fig. 2.8. Time series of seasonal anomalies of the LS as the median of the various datasets, with respect to 1979–88 (black). The three warm events are volcanically induced (Agung, El Chichón, and Mt. Pinatubo, respectively). The red and blue lines represent the highest and lowest values, respectively, reported by any of the sources.**

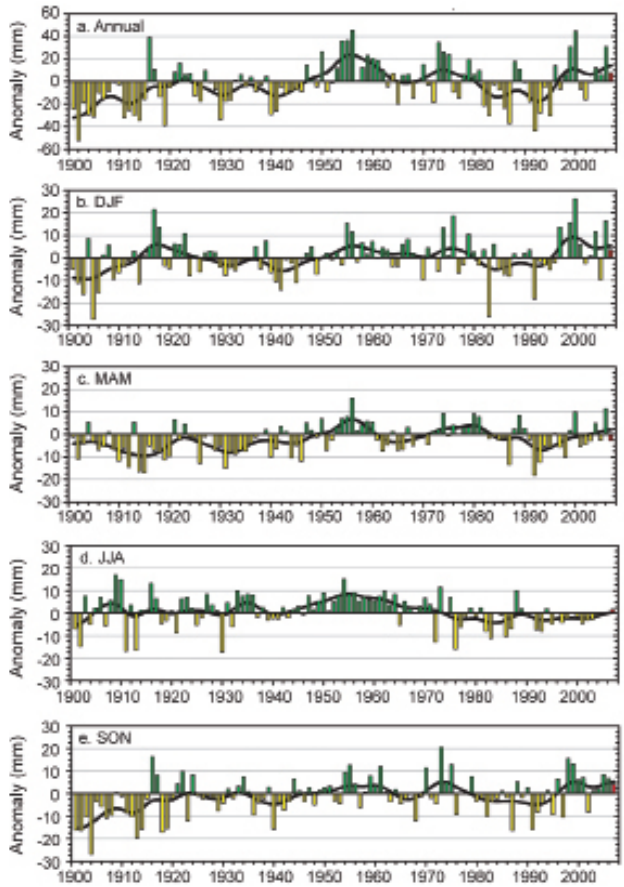


**Fig. 2.9. Time series of annual and seasonal global land surface precipitation anomalies (mm) over the period 1900–2007, based on observations from the Global Historical Climatology Network dataset (Vose et al. 1992): (a) annual, (b) Dec–Feb, (c) Mar–May, (d) Jun–Aug, and (e) Sep–Nov. The precipitation anomalies were calculated with respect to the 1961–90 base period mean: green bars = positive anomalies, yellow bars = negative anomalies, and red bar = 2007 anomaly. In addition, the black line in each time series denotes the smoothed annual or seasonal values using a 13-point binomial filter.**

nificantly less than in 2006 when the annual value was the eighth wettest (~31 mm above average) since the beginning of the twentieth century.

From a seasonal perspective, only the March–May period (boreal spring) was drier than average globally, with an anomaly of –2.7 mm (–1.1%) below the mean (Fig. 2.9c). Of special note, the global anomaly for the June–August period (boreal summer) was +1.67 mm (+0.6%), which was the largest positive precipitation anomaly for that season since 1994. In fact, of the past 15 yr only 2007 had above average precipitation globally during the June–August period. In contrast, 9 of the past 10 yr have been wetter than average during September–November (Fig. 2.9e), and 2007 continued this pattern with a global anomaly of +4.2 mm (+1.7%) above the long-term mean.

From a hemispheric perspective, the Southern Hemisphere was drier than average for the year (–20 mm, –1.7%), while the Northern Hemisphere was wetter than average (+18.4 mm, +2.2%) in 2007 (not shown). The seasonal variations reflected these annual anomalies, with only the December–February season (austral summer) wetter than average in the Southern Hemisphere (+25.9 mm), while the same 3-month period (boreal winter) was drier than average in the Northern Hemisphere (–5.2 mm, –6.3%). The summer (June–August) was anomalously wet in the Northern Hemisphere (+11.7 mm, +3.7%), which was only the eighth time in the past 20 yr with above average precipitation.

Regional-scale precipitation patterns in 2007 were influenced by the El Niño–Southern Oscillation, as the year began with a weak El Niño event and ended in a moderate-to-strong La Niña episode. Precipitation patterns during the period December 2006 to February 2007 were in a number of places consistent with El Niño (warm event) conditions (Ropelewski and Halpert 1987). Dry conditions occurred across much of Australia, the islands of the western tropical Pacific, and Hawaii, while wet conditions were observed in parts of central South America (Bolivia, southern Brazil, northern Argentina, Uruguay and Paraguay). Additional details on ENSO conditions are available in section 4b.

In the central United States, unusually wet conditions intensified during March–May, generating widespread flooding across the southern plains. The excessive rainfall in the region persisted into summer

(June–August), and both Oklahoma and Texas had their wettest summer on record (historical records began in 1895). Excessive rainfall and flooding also affected large areas of the United Kingdom during the summer, and a number of long-term rainfall records were broken. In southern Australia, long-term rainfall deficits continued during the austral winter (June–August), where over six years of drought has affected the Murray–Darling basin (see chapter 6 for additional details). The tropical western North Pacific was significantly wetter than average during September–November 2007, especially the Philippines and Borneo, which contributed to the wetter-than-average seasonal anomaly for the Northern Hemisphere during that period (~11 mm).

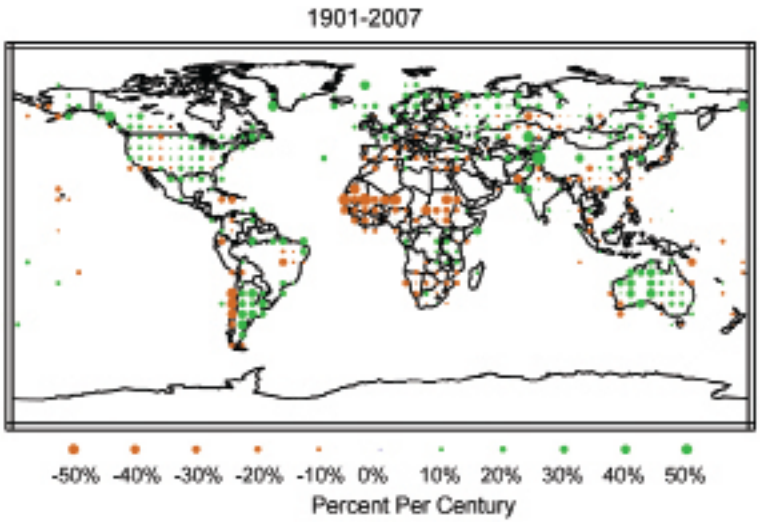


**Fig. 2.10. Annual precipitation trends for the period 1901–2007 depicted in the percent change per century. Calculation of grid cell trends required at least two-thirds (66%) of the years without missing data. Stations with more than one-third of their data missing during the 1961–90 reference period were excluded from the analysis.**

The wetter-than-average global conditions in 2007 are consistent with a long-term increasing trend in precipitation. Global land surface precipitation has increased approximately 2% since the start of the twentieth century, with the greatest contribution to this rise occurring in mid- and high-latitude regions (Fig. 2.10). Although there has been pronounced decadal variability, with all regions of the world experiencing multiyear periods of both increasing and decreasing trends during the past century, the overall trend has been toward greater precipitation amounts in much of the world. A notable exception has occurred in the Northern Hemisphere tropics, where rainfall has decreased at a rate near 0.8% per decade, largely due to a recent multidecadal period of drier-than-average conditions in western and eastern Africa.

In many places, the positive precipitation trends also have been accompanied by even larger increases in heavy and extreme precipitation events, as warming temperatures have increased the water-holding capacity of the atmosphere (Trenberth et al. 2003). In the United States, for example, the amount of precipitation falling in the heaviest 1% of rain events has increased by 20% during the twentieth century, while total precipitation has increased by only 7% (Groisman et al. 2004). Similar trends have occurred in other regions of the world, as precipitation from heavy events has increased while light-to-moderate events have exhibited much less change (Groisman et al. 2005).

*(ii) Over oceans*—P. Xie and J. E. Janowiak

Real-time monitoring of global oceanic precipitation is routinely conducted at NOAA's CPC with the use of the rain gauge–satellite merged "CAMS-OPI" dataset (Janowiak and Xie 1999). By combining gauge observations of precipitation collected and archived by CPC via the CAMS (Ropelewski et al. 1985) with the satellite-based OPI (Xie and Arkin 1998), the CAMS-OPI provides monthly precipitation estimates over global land and ocean on a real-time basis. As shown in Fig. 2.11 (middle panel), several large-scale anomalies (departures from normal) were observed over the global oceans, which are discussed below.

The mean precipitation amount over the global oceans during 2007 (Fig. 2.11, top panel) was 2.890 mm day$^{-1}$, which is equivalent to a freshwater influx of 1040.3 Kg m$^{-2}$. This was an increase over 2006, when the global mean was 2.812 mm day$^{-1}$ and the equivalent freshwater influx was 1,026.4 Kg m$^{-2}$. Maximum annual precipitation rates of over 9 mm day$^{-1}$ are observed during the year over the tropical western Pacific where the ITCZ merges with the SPCZ near the equator and 150°E, and over the tropical eastern Indian Ocean. Meanwhile, relatively light precipitation was recorded, as expected, over the oceanic dry zones in the southeast Pacific, northeast Pacific off the coast of the southwestern United States, southeast Atlantic, tropical North Atlantic near western Africa, and the southeastern Indian Ocean.

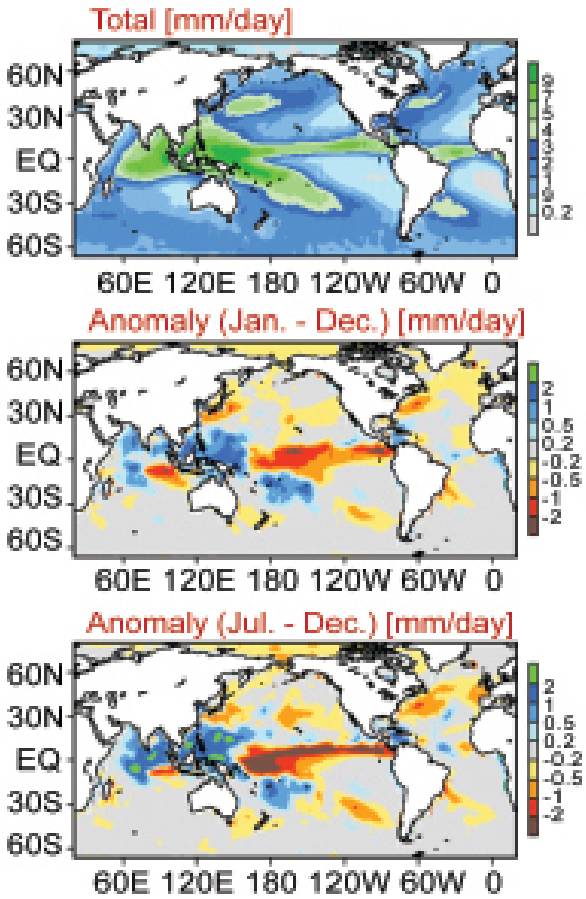


**Fig. 2.11. (top) Annual mean total precipitation (mm day$^{-1}$), (middle) annual mean precipitation anomaly (mm day$^{-1}$), and (bottom) Jul–Dec precipitation anomaly (mm day$^{-1}$) for 2007 as observed by the gauge-satellite merged dataset of CAMS-OPI (Janowiak and Xie 1999). Precipitation anomalies were calculated using 1979–95 as the base period.**

Over the tropical Pacific, the 2006/07 El Niño ended abruptly in February 2007. Negative SST anomalies expanded from the equatorial eastern Pacific and developed into a moderate-to-strong La Niña during the second half of the year (Climate Prediction Center 2007). Associated with the evolution of this La Niña event, the precipitation anomaly for 2007 exhibited a canonical horseshoe-shaped distribution pattern (Ropelewski and Halpert 1989; Xie and Arkin 1997), with depressed precipitation over the equatorial eastern and central Pacific surrounded by enhanced precipitation over the western Pacific and central South Pacific (Fig. 2.11, middle and bottom panels).

Over the Indian Ocean, the precipitation distribution during 2007 was characterized by a large positive precipitation anomaly over the northern portion of the ocean. This strong precipitation anomaly is associated with the intensified Asian monsoon circulation observed during summer 2007, as indicated by the South Asian monsoon index of Goswami et al. (1999). Hurricane activity over the Atlantic Ocean was close to normal during 2007, with a total of 17 tropical storms and 5 hurricanes recorded. Two category 5 hurricanes (Dean and Felix) passed through the Caribbean Sea, contributing to the above normal precipitation anomaly over the region during the second half of the year. Precipitation deficits were observed over the northwestern Atlantic Ocean off the North America continent.

Strong precipitation variations at intraseasonal time scales were recorded over the eastern Indian Ocean and western Pacific during November and December 2007 (Fig. 2.12). A positive precipitation anomaly of larger than 5 mm day$^{-1}$ progressed eastward from the central equatorial Indian Ocean to the date line. These intraseasonal variations were associated with MJO (Madden and Julian 1971) activity, which in 2007 exhibited the strongest intensity in the past 4–5 yr (Climate Prediction Center 2008).

### 2) Northern Hemisphere continental snow cover extent—D. A. Robinson

Annual SCE over Northern Hemisphere lands averaged 24.0 million km$^2$ in 2007, a decrease of 0.9 million km$^2$ compared with the 2006 annual mean. This is 1.5 million km$^2$ less than the 38-yr average and ranks 2007 as having the third least extensive cover of record (Table 2.2). This evaluation considers snow over the continents, including the Greenland ice sheet. The SCE in 2007 ranged from 45.3 million km$^2$ in January to 2.0 million km$^2$ in August. Monthly snow extent values are calculated at the Rutgers Global Snow Lab[1] from weekly SCE maps produced by NOAA meteorologists, who rely primarily on daily visible satellite imagery to construct the maps (Robinson and Frei 2000).

Hemispheric SCE was below the long-term mean in every month except December. Departures were as large as –3.0 million km$^2$ in May, followed closely by June (–2.6) and April (–2.5). In conjunction with the lower than average extents in most of 2006, the 12-month running means of Northern Hemisphere extent were below the long-term average throughout

[1] Maps depicting daily, weekly, and monthly conditions, daily and monthly anomalies, and climatologies for the entire period of record may be viewed at the Rutgers Global Snow Lab Web site (http://climate.rutgers.edu/snowcover).

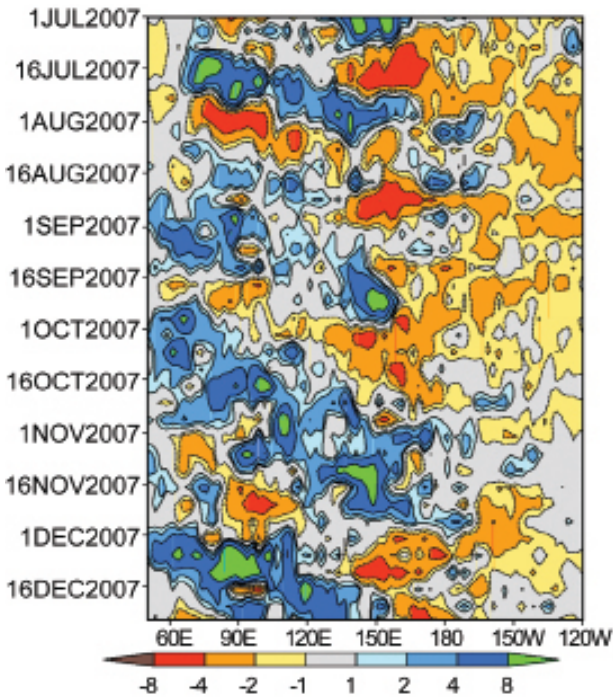


**Fig. 2.12. Time–longitude section of precipitation anomaly averaged over the tropical Pacific (5°S–5°N) as observed by the GPCP pentad precipitation dataset (Xie et al. 2003). Precipitation anomaly is calculated using 1979–95 as the base period.**

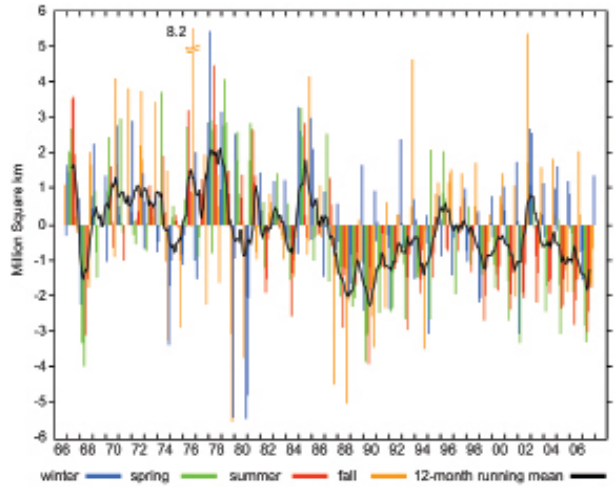


**Fig. 2.13. Anomalies of monthly snow cover extent over Northern Hemisphere lands (including Greenland) between Nov 1966 and Dec 2007. Also shown are 12-month running anomalies of hemispheric snow extent, plotted on the seventh month of a given interval. Anomalies are calculated from NOAA snow maps. Mean hemispheric snow extent is 25.5 million km$^2$ for the full period of record. Monthly means for the period of record are used for nine missing months between 1968 and 1971 to create a continuous series of running means. Missing months fall between Jun and Oct, and no winter months are missing.**

the year (Fig. 2.13). In fact, the negative 12-month anomaly at years end had not been reached since the record lows of the satellite era were observed during 1988–90. Eurasian SCE was well below the long-term average in 2007 and ranked as the second least extensive cover of the satellite era. North American SCE was similar, ranking the eighth least extensive.

The 2007 SCE exhibited some variability on temporal and spatial scales. Eurasian SCE was at near record lows until the fall, when extents came close to the long-term average. North American SCE was above average in January and February, but fell below average in March, a tendency that persisted through November. December cover over North America was the third most extensive, the major factor contributing to the ninth most extensive ranking over Northern Hemisphere land areas. Spring and summer snow cover continues to be less extensive in the second half of the satellite record than in the first half, with 2007 spring SCE the third lowest on record (Fig. 2.14).

Over the contiguous United States, SCE was above average in January and February and well below average the remainder of the year, with the exception of December, which was third most extensive. Alaskan snow cover ran well below average from April through September, and was relatively close to average from October through December.

### 3) Global cloudiness—A. T. Evan, A.K. Heidinger, Y. Liu, and B. Maddux

#### *(i) Introduction*

Global patterns of cloudiness in 2007 were largely dominated by modest fluctuations in ENSO, which consisted of a positive anomaly during the beginning of the year that was followed by the development of a negative one in the boreal fall. While high cloud cover anomalies associated with even weak ENSO events can be upward of 20% across the tropical Pacific, none of the observed cloudiness anomalies associated with the ENSO events of 2007 represented a statistically significant departure from the mean state (here, a statistically significant departure from average is estimated as an anomaly that is more than two standard deviations from the climatological mean). With that being said, the Arctic and the Amazon basin and its environs both exhibited strong deviations in total cloud cover over 2007 (see Figs. 2.15–2.17), which may have resulted from changes in atmospheric moisture and surface temperatures (for the case of the Arctic) and land use change (for the case of the Amazon).

**Table 2.2. Monthly and annual climatological information on Northern Hemisphere and continental snow extent between Nov 1966 and Dec 2007. Included 2007 values and rankings. Areas are in millions km$^2$. Years 1968, 1969, and 1971 have one, five, and three missing months, respectively, and thus are not included in the annual (Ann) calculations; North America (N. Am.) includes Greenland. Ranks are from most extensive (1) to least (ranges from 38 to 42 depending on the month).**

| | Years | Mean | Std dev | 2007 | 2007 Northern Hemisphere rank | Eurasia rank | N. Am. rank |
|---|---|---|---|---|---|---|---|
| Jan | 41 | 46.9 | 1.5 | 45.3 | 38 | 40 | 14 |
| Feb | 41 | 45.9 | 1.8 | 45.2 | 28 | 33 | 12 |
| Mar | 41 | 41.0 | 1.8 | 39.6 | 33 | 31 | 29 |
| Apr | 41 | 31.3 | 1.7 | 28.8 | 39 | 40 | 27 |
| May | 41 | 20.4 | 1.9 | 17.4 | 40 | 38 | 37 |
| Jun | 40 | 10.9 | 2.1 | 8.3 | 38 | 39 | 29 |
| Jul | 38 | 4.8 | 1.5 | 2.8 | 38 | 36 | 37 |
| Aug | 39 | 3.5 | 1.0 | 2.0 | 39 | 38 | 39 |
| Sep | 39 | 5.6 | 1.0 | 4.1 | 37 | 37 | 34 |
| Oct | 40 | 18.3 | 2.6 | 16.4 | 33 | 33 | 26 |
| Nov | 42 | 34.1 | 2.0 | 33.4 | 29 | 27 | 29 |
| Dec | 42 | 43.5 | 1.8 | 44.6 | 9 | 25 | 3 |
| | | | | | | | |
| Ann | 38 | 25.5 | 1.0 | 24.0 | 36 | 37 | 31 |

*(ii) Data description*

To investigate the global pattern of cloudiness in 2007, we use the long-term cloud climatology from the AVHRR from the Pathfinder Atmospheres Extended (PATMOS-x) project (PATMOS-x data acquired from http://cimms.ssec.wisc.edu/clavr/patmosx.html). Cloud cover extent is defined as the percentage of 4-km pixels that are cloudy within each 55-km grid cell. Cloud is detected within each pixel through the use of spatial and spectral tests. PATMOS-x results are available twice daily from each operational NOAA satellite from 1981 to 2007.

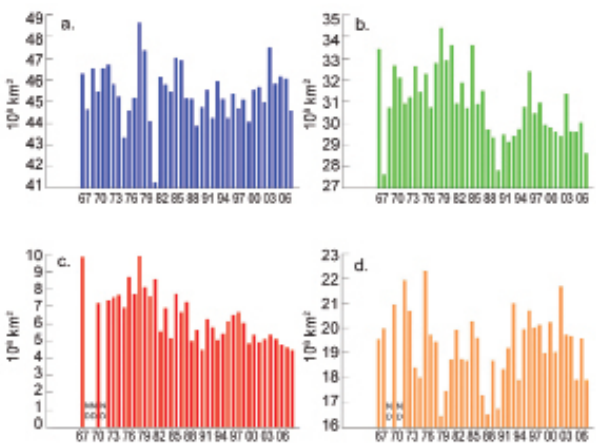


**Fig. 2.14. Extent of (a) winter (DJF), (b) spring (MAM), (c) summer (JJA), and (d) autumn (SON) seasonal snow cover over Northern Hemisphere lands (including Greenland) from the winter of 1966–67 through the autumn of 2007.**

*(iii) Amazon basin and environs*

There was a strong negative anomaly in cloud cover over northern Bolivia, parts of Paraguay, and much of Brazil (Fig. 2.15). This anomaly was largely confined to regions surrounding the dense tropical forests of the Amazon basin, along the so-called arc of deforestation, and the agricultural lands farther to the south and east. For the most part the decreases in cloudiness that were statistically significant were on the order of 5% to 10%. According to data from the *Terra* MODIS instrument, aerosol cover in 2007 over this same region was the highest on record (Evan 2008), and is an indication of fire activity in these same areas (Koren et al. 2007). Heavy smoke cover has an adverse effect on cumulus cloud development

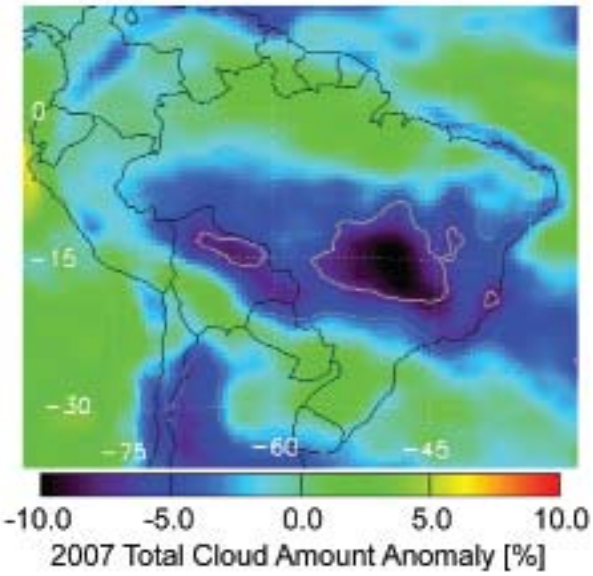


**Fig. 2.15. Total cloud cover anomaly for 2007 over Brazil. The thin gray contour represents anomalies that are one standard deviation from the climatological mean value, and the thick gray contour represents anomalies that are two standard deviations from the mean state.**

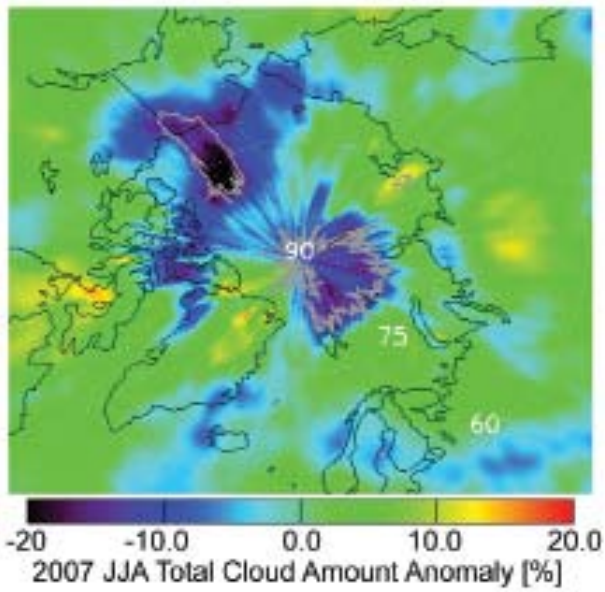


**Fig. 2.16. Total Arctic summer cloud cover anomaly 2007. Cloud cover anomaly for the months of Jun, Jul, and Aug over the northern polar regions. The thick gray contour represents anomalies that are two standard deviations from the mean state.**

directly via warming, and therefore stabilization, of the boundary layer, and indirectly via reductions in surface heating and evapotranspiration (Koren et al. 2004). The same pattern and intensity of the total cloud cover anomaly is not repeated for high cloud cover, but this is not surprising since most deep convection occurs in the more central regions of the Amazon basin.

*(iv) Arctic*

Figure 2.16 is a map of the Arctic summer total cloud cover anomaly. There were widespread negative anomalies in cloudiness that extended north from Alaska, and around much of the pole, representing deficits in cloudiness of 10% to 20%. According to data from the NCEP–NCAR reanalysis (data acquired from www.cdc.noaa.gov/) (Kalnay et al. 1996), during the boreal summer months there existed a strong high pressure anomaly over much of the western Arctic (sea level pressure and 500-hPa geopotential heights; not shown). It is likely that this high pressure directly contributed to the reduction of cloudiness over the same time period. There has been a long-term upward trend in Arctic cloud cover during the spring and summer that is thought to be associated with surface warming in the same region (Wang and Key 2003). It is possible that discontinuation of this general cloud cover trend in 2007 is also linked to summertime surface temperatures in this same region (Wang and Key 2003), as data from the NCEP reanalysis do not show a strong positive anomaly for temperatures at the surface in 2007 (not shown here).

Although this high pressure anomaly did persist into the fall, the summertime cloud cover deficit gave way to a strongly positive cloudiness anomaly that was much more spatially expansive, particularly in the eastern Arctic (Fig. 2.17). Here, the region of above average cloudiness extended northward from much of Siberia, and the Bering Strait, and for the most part consisted of increases in cloudiness that are upward of 30%. There has been a modest downward trend in Arctic cloud cover during autumn (Wang and Key 2003), which may be linked to decreases in moisture convergence for the same region (Liu et al. 2007). At the same time, according to NCEP reanalysis data, in 2007 an anomalously low sea level pressure over the eastern Arctic and resulting northward flow penetrated the Arctic from North America and the North Pacific (850-hPa vector winds). Surface temperatures in the region of the positive cloud anomalies were also above average. Therefore, it is likely that the northerly flow, possibly combined with a warmer surface, strongly encouraged cloud development here.

However, there may also be a linkage between the positive cloud anomaly and the negative sea

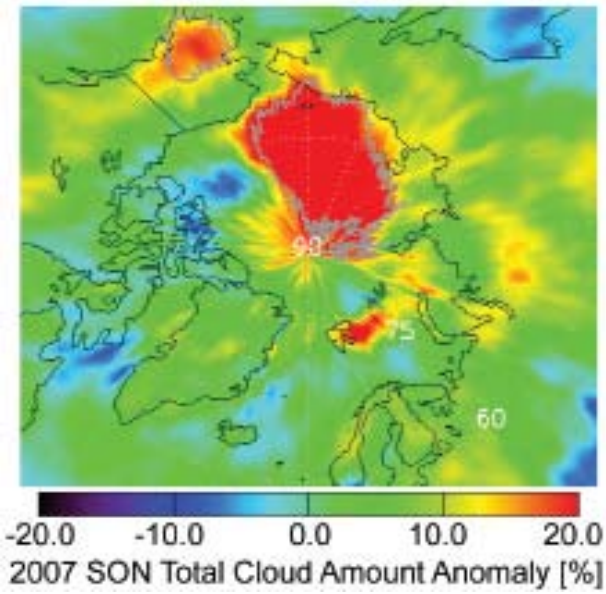


**Fig. 2.17. Total Arctic autumn cloud cover anomaly in 2007. Cloud cover anomaly for the months of Sep, Oct, and Nov over the northern polar regions. The thick gray contour represents anomalies that are two standard deviations from the mean state.**

ice extent anomaly over the eastern Arctic Ocean. Data from the CloudSat cloud profiling radar and the CALIPSO instruments show that during 2007, low clouds had somewhat lower base heights, but midlevel cloud amount increased. The increase in the midlevel cloud might in part be a result of an increase in the vertical extent of the low-level clouds associated with the less stable atmosphere of the open water region.

Since cloud detection with the AVHRR over ice is difficult, it is possible that the anomalies in cloudiness here are artifacts of the cloud detection methodology that are initiated by changes in sea ice. Therefore, the above analysis was also repeated with the MODIS cloud climatology (data acquired from http://daac.gsfc.nasa.gov) (Platnick et al. 2003), since this 36-channel imager is better suited for cloud detection over ice. Analysis of these data showed very similar results, suggesting that the anomalies are robust.

### *d. Trace gases and aerosols*

#### 1) Carbon dioxide—R. C. Schnell

$CO_2$ emitted from fossil fuel burning is partitioned into three mobile reservoirs: the atmosphere, oceans, and terrestrial biosphere. One result of fossil fuel combustion has been that atmospheric $CO_2$ has increased from about 280 ppm (ppm = parts in $10^6$ by dry-air mole fraction) at the start of the industrial revolution to more than 380 ppm today.[2] Since high-accuracy measurements began more than 50 yr ago, ~57% of the emitted $CO_2$ has remained in the atmosphere and the remainder has gone into two "sinks," oceans and land biosphere (which include plants and soil carbon).

Currently, more than 8 Pg (Pg = $10^{15}$g) of carbon is emitted to the atmosphere by fossil fuel combustion each year (Marland et al. 2007). Global emissions have increased since 2000, surpassing even the most pessimistic of the IPCC emission scenarios used to test climate models. During the 1990s, net uptake by the oceans was estimated as 1.7 ± 0.5 Pg $yr^{-1}$ and by the land biosphere as 1.4 ± 0.7 Pg $yr^{-1}$ (Prentice et al. 2001). The gross fluxes between atmosphere and oceans, and atmosphere and terrestrial biosphere (photosynthesis and respiration), are approximately 100 Pg $yr^{-1}$. Interannual variations in the atmospheric increase of $CO_2$ (see Fig. 2.18a, based on Conway et al. 1994) are due to small changes in these net fluxes, and not due to variations in fossil fuel emissions. Most attempts to explain the interannual variability of the atmospheric $CO_2$ increase have focused on short-term climate fluctuations (e.g., ENSO and post-Pinatubo cooling), but the mechanisms, especially the role of the terrestrial biosphere, are not well understood. To date, about 5% of conventional fossil fuels have been combusted. If combustion were stopped today, after a few hundred years, 15% of the total carbon emitted would remain in the atmosphere, and the remainder would be in the oceans (Maier-Reimer and Hasselmann 1987).

The preliminary globally averaged atmospheric $CO_2$ mole fraction in 2007 was 382.7 ppm, which was ~1.8 ppm greater than the 2006 global annual mean (380.9 ppm). While an average annual increase of 1.6 ppm $yr^{-1}$ has occurred since 1980, the average rate of increase since 2000 has been 1.9 ppm $yr^{-1}$. This suggests that the fraction of $CO_2$ emitted from sources that remain in the atmosphere may be increasing.

Because of the policy implications surrounding

[2] Note that fossil fuels are primarily responsible for the observed increase in $CO_2$ over the past half century. In the nineteenth century, land use change emissions dominated, but since ~1940 cumulative $CO_2$ emissions from fossil fuel burning overtook cumulative emissions from land use change (Marland et al. 2007). Approximately 87% of fossil fuel emissions have occurred since 1940, and currently the terrestrial biosphere is a small net sink.

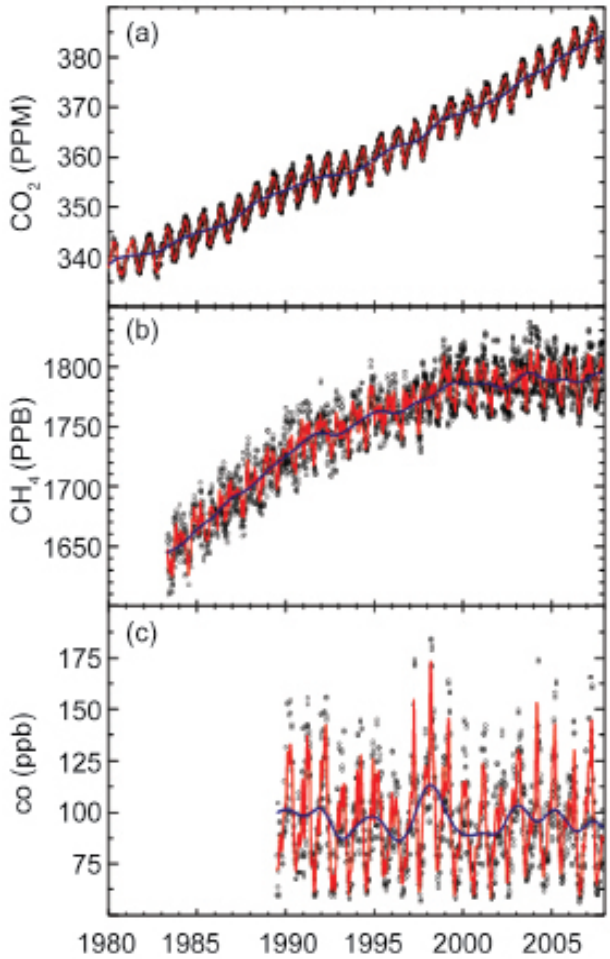


**Fig. 2.18. Trace gas mole fractions (black symbols) determined from weekly discrete samples collected at the NOAA/ESRL Mauna Loa Observatory for (a) $CO_2$ (courtesy: T. J. Conway, NOAA), (b) $CH_4$ (courtesy: E. J. Dlugokencky, NOAA), and (c) CO (courtesy: P. C. Novelli, NOAA). In all panels, the solid blue line is the deseasonalized trend and the red line is a smooth curve fitted to the black symbols. (Current $CO_2$ trends at MLO are available online at www.esrl.noaa.gov/gmd/ccgg/trends/. Additional plots can be found online at www.esrl.noaa.gov/gmd/ccgg/iadv/ and www.esrl.noaa.gov/gmd/Photo_Gallery/GMD_Figures/ccgg_figures/.)**

the fate of fossil fuel $CO_2$, NOAA/ESRL launched "Carbon Tracker," a new tool that uses observations and a state-of-the-art model to keep track of time-dependent emissions and uptake of atmospheric $CO_2$, from both natural and anthropogenic processes. For the period January 2001 to December 2006, Carbon Tracker (available online at http://carbontracker.noaa.gov) estimated that uptake of carbon by North American ecosystems averaged –0.65 Pg C $yr^{-1}$, varying between –0.4 and –1.00 Pg C $yr^{-1}$ (Peters et al. 2007); this can be compared to the total North American fossil fuel emissions of 1.9 Pg C $yr^{-1}$.

### 2) Methane—R. C. Schnell and E. Dlugokencky

Methane's contribution to anthropogenic radiative forcing, including direct and indirect effects, is about 0.7 W $m^{-2}$, about half that of $CO_2$. Changes in the burden of methane also feed back into atmospheric chemistry, affecting the concentrations of OH and $O_3$. The increase in methane since the preindustrial era is responsible for approximately one-half the estimated increase in background tropospheric $O_3$ during that time. Changes in OH concentration affect the lifetimes of other greenhouse gases such as the replacement refrigerants (HFCs, HCFCs).

High-precision measurements of atmospheric methane provide climate modelers with current and past rates of $CH_4$ increase, and they are also useful in constraining the global $CH_4$ budget, and how it is changing with time. This "top-down" approach can determine total global emissions to within ±10%, but background atmospheric observations alone can not effectively quantify emissions from individual sources. A recent surprise in the global $CH_4$ budget was the report that vegetation can be a significant source of atmospheric $CH_4$, even under aerobic conditions (Keppler et al. 2006), but the original emission estimates are likely overestimated. (The inability to identify this source sooner shows the limitations of the observations, particularly in the tropics, for quantifying weakly emitting, diffuse sources.)

In Fig. 2.18b, $CH_4$ mole fractions from the NOAA observatory at Mauna Loa, Hawaii, are plotted as a function of time. During more than 20 yr of measurements, $CH_4$ has increased by nearly 10%, but the rate of increase has slowed in recent years. A large increase in 1998 and a smaller one in 2003 were likely the result of climatic conditions that resulted in increased emissions from biomass burning and natural wetlands. Otherwise, atmospheric $CH_4$ has remained nearly constant since the late 1990s (Dlugokencky et al. 2003). Possible causes for the recent lack of growth in atmospheric $CH_4$ burden are decreased emissions from natural wetlands because of widespread drought in the tropics (Bousquet et al. 2006) and a change in the $CH_4$ sink because of increased lightning (Fiore et al. 2006), but the exact causes are still unclear. The preliminary 2007 global annual $CH_4$ average of 1782.2 ppb is 7 ppb greater than the concentration observed in 2006. The reasons for the increase in 2007 are not yet known, but analysis of CO measurements suggests it is not from biomass burning.

### 3) Carbon monoxide—R. C. Schnell

Unlike $CO_2$ and $CH_4$, carbon monoxide does not

strongly absorb terrestrial IR radiation, but it still impacts climate through its chemistry. The chemistry of CO affects OH (which influences the lifetimes of $CH_4$ and HFCs) and tropospheric $O_3$ (itself a greenhouse gas), so emissions of CO can be considered equivalent to emissions of $CH_4$ (Prather 1996). Current emissions of CO may contribute more to radiative forcing over decadal time scales than emissions of anthropogenic $N_2O$ (Daniel and Solomon 1998).

Carbon monoxide mole fractions from Mauna Loa (symbols) are plotted as a function of time in Fig. 2.18c and show little trend over the period of these measurements (Novelli et al. 2003). Superimposed on the flat trend are significant increases during 1997 to 1998, and again in 2002 to 2003, which were likely the result of tropical (Langenfelds et al. 2002) and boreal biomass burning (Kasischke et al. 2000). Since the lifetime of CO is relatively short (few months), the anomaly quickly disappeared and CO returned to pre-1997 levels shortly afterward. In 2007, CO levels are comparable to those found in the early 2000s.

The preliminary globally averaged CO mole fraction in 2007 was 84.0 ppb, 2 ppb greater than the 2006 global annual mean, and 11 ppb lower than 1998, which had a large contribution from CO that was emitted by biomass burning.

#### 4) Halocarbons—R. C. Schnell and S. A. Montzka

*Decreases in ozone-depleting gases and their replacements*

Long-lived halocarbons affect the radiative balance of the atmosphere because they efficiently absorb terrestrial IR radiation (see section 2d5). Long-lived halocarbons containing bromine and chlorine also influence the radiative atmospheric balance indirectly through their destruction of stratospheric ozone.

Because of concern over stratospheric ozone depletion, production of many halocarbons has become restricted over the past two decades. The phase out of human-produced halocarbons internationally was brought about through amendments and adjustments to the 1987 Montreal Protocol on Substances that Deplete the Ozone Layer. As a result of these efforts, mixing ratios of most of the potent ozone-depleting gases have been declining at the Earth's surface in recent years. These declines continued in 2007 as shown in Fig. 2.19. Of the main ozone-depleting substances measured in the global NOAA/ESRL sampling network and not considered to be replacement chemicals, only H-1301 was still increasing in the background atmosphere in 2007.

The NOAA/ESRL data show that mixing ratios of some halogenated gases continue to increase globally (Fig. 2.19). The most rapid increases are observed for HCFCs and HFCs, which are chemicals commonly used as replacements for chlorofluorocarbons (CFCs), halons, and other ozone-depleting gases. Although HCFCs contain chlorine and deplete ozone with a reduced efficiency compared to CFCs, HFCs do not participate in ozone-destroying reactions.

Increases in HCFCs have continued so that by mid-2007 chlorine accounted for by the three most abundant HCFCs amounted to 237 ppt, or 8.8% of all chlorine carried by long-lived halocarbons of anthropogenic Chlorine (not including Cl from $CH_3Cl$). Mixing ratios of HFC-134a, the most abundant HFC in the global background atmosphere, increased nonlinearly in the 1990s during the period of early production and use. From 2004 through 2007, however, it increased in the global troposphere at a fairly constant linear rate of 4.5 (±0.3) ppt $yr^{-1}$. Concern over increases in HFCs stems in large part because these gases are efficient absorbers of infrared radiation.

The influence of these disparate trends on future levels of stratospheric ozone can be gauged roughly from a sum of Cl and Br in long-lived halocarbons provided the enhanced efficiency for Br to destroy ozone is considered (note that this efficiency factor has been updated here to 60 based upon a reanalysis appearing in the latest WMO Scientific Assessment of Ozone Depletion (Clerbaux and Cunnold et al. 2007). This sum is expressed here as EECl (Fig. 2.19) and is derived from surface-based measurements. EECl provides an estimate of the ozone-depleting power of trace gases a few years in the future, when air at Earth's surface will have become mixed into the midlatitude stratosphere where the ozone layer resides. A second metric, ECl, provides an estimate of the ozone-depleting power of trace gases in the near future for the stratosphere over the polar regions (not shown).

The observations indicate that through 2007 the ECl and EECl content of the lower atmosphere declined fairly steadily since the peak in 1994 at a mean rate of 25 to 28 ppt $yr^{-1}$. Scenarios projecting future halocarbon mixing ratios have been derived elsewhere based upon full compliance with the fully amended and revised Montreal Protocol and our understanding of atmospheric lifetimes of these gases (Clerbaux and Cunnold et al. 2007). These analyses suggest that it will take 40 to 60 yr for EECl and ECl to decline to the levels present in 1980, which is before ozone depletion was first observed. This 1980 level is notable, given that one might expect nearly full recovery of stratospheric ozone once atmospheric EECl or ECl returns back to this level. The time scale for ozone recovery

will depend upon other factors as well, however, such as stratospheric temperatures and atmospheric aerosol loading. Nonetheless, the declines in EECl from 1994 to the present time represent a significant drop in the atmospheric EECl burden; as of 2007 EECl had declined 26% of the way back down to the 1980 level (lower panel of Fig. 2.19).

Progress toward EECl returning to the abundance in 1980 can be readily assessed with the NOAA ODGI (see www.cmdl.noaa.gov/odgi/). This index is derived from EECl and ECl data for the midlatitude and Antarctic stratosphere. The index is scaled so that a value of 100 represents the EECl or ECl abundance at its peak, and 0 represents the 1980 level (the level at which no ozone depletion is expected assuming constancy in all other variables). In 2007 the ODGI-Midlatitudes was 73.4, indicating that the abundance of ozone-depleting substances have decreased over 26% of the way toward the levels that were present in 1980 (Fig. 2.19). Less progress is evident for Antarctica where the ODGI-Antarctica was 86.0 in 2007. This suggests halocarbon abundances have declined slightly more than 14% of the way toward 1980 levels.

Changes in the direct radiative influence of long-lived halocarbons can be estimated from observed changes in atmospheric mixing ratios with knowledge of trace gas radiative efficiencies. Such an analysis suggests that the direct radiative forcing of these gases was still increasing in 2007, though at a much slower rate than observed from 1970 to 1990 (see below).

### 5) Nitrous oxide and sulfur hexafluoride—J. W. Elkins and G. S. Dutton

Nitrous oxide and $SF_6$ absorb infrared radiation in the atmospheric window (8 to 14 μm) and contribute to the radiation budget of the Earth's surface. NOAA/ESRL scientists have been measuring their mixing ratios on the same channel of electron-capture gas chromatographs using both in situ and flask sam-

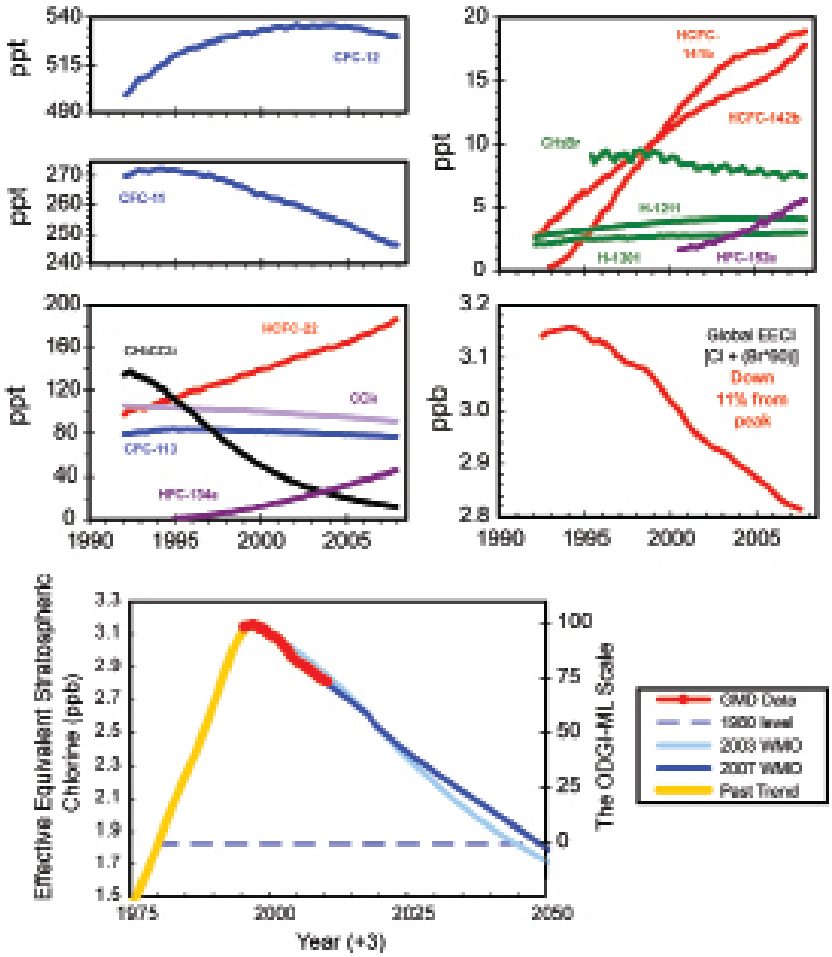


**Fig. 2.19. Changes in global mean tropospheric mixing ratios (in ppt or pmol mol$^{-1}$) of the most abundant CFCs, HCFCs, HFCs, chlorinated solvents, and brominated gases. These global changes are estimated from atmospheric measurements made at remote sites in both the Northern and Southern Hemispheres (from the NOAA/ESRL Cooperative Air Sampling Network). The middle right-hand panel shows secular changes in atmospheric equivalent chlorine (EECl; in ppb or nmol mol$^{-1}$), which is an estimate of the ozone-depleting power of atmospheric halocarbons. EECl is derived from observed mixing ratios of ozone-depleting gases appearing in the other four panels, and it is derived from the sum of [Cl + (Br×60)] contained in these gases. The bottom panel shows the recent changes in EESC observed by the NOAA/ESRL global network relative to the secular changes observed in the past, including the level observed in 1980 when the ozone hole was first observed, and a projected future. The Ozone Depleting Gas Index for midlatitudes is derived (right-hand axis) from rescaling EESC. EESC is derived from EECl by simply adding 3 yr to the time axis to represent the lag associated with mixing air from the troposphere to the middle stratosphere, where the ozone layer resides. [Source: Montzka et al. (1996, 1999).]**

pling since 1977 for $N_2O$ and since 1995 for $SF_6$. On a per molecule basis, $N_2O$ is about 298 times and $SF_6$ is about 22,800 times more effective than carbon dioxide as a greenhouse gas (Forster et al. 2007, p. 212). The global mean mixing ratios at the end of 2007 for $N_2O$ was 321.4 ppb while $SF_6$ was 6.29 ppt (Fig. 2.20). The atmospheric concentrations of these potent infrared absorbers, $N_2O$ and $SF_6$, are approximately 1,000 and 60 million times less than atmospheric $CO_2$ (382.7 ppm), respectively. But since the beginning of the industrial revolution, increases in the burden of atmospheric $N_2O$ have added 0.16 ± 0.02 W $m^{-2}$, and increases in $SF_6$ have added 0.0029 W $m^{-2}$ to the Earth's surface radiation budget (Forster et al. 2007, p. 141). Atmospheric $N_2O$ also is involved in stratospheric $O_3$ depletion, because it is a major source of stratospheric NO that forms nitrogen dioxide quickly, which in turn destroys $O_3$ in a catalytic cycle.

Like $CO_2$, $N_2O$ and $SF_6$ have been growing at a relatively linear rate of 0.778 ± 0.003 ppb $yr^{-1}$ since 1977 and 0.218 ± 0.001 ppt $yr^{-1}$ since 1995 as shown in Fig. 2.20 (top panel). Sulfur hexafluoride is the sixth fastest growing greenhouse gas in percentage of all Montreal and Kyoto Protocol gases since 1998. Examining the instantaneous growth rates, there exist variations of greater than ±25% throughout their respective periods for both gases shown at the bottom of Fig. 2.20. The growth rate of $SF_6$ increased to a high of 0.28 ppt $yr^{-1}$ in mid-2007, however, more data are required to determine if this increased growth will be sustained in the subsequent year. The growth rate of $N_2O$ exhibits considerable inter-annual changes that may result from transport or changes in the magnitudes of emissions. The budget of atmospheric $N_2O$ is about 30% out of balance because of major anthropogenic sources from the application of nitrogen fertilizers on crops, by products of chemical manufacturing processes, and catalytic reduction of oxides of nitrogen generated from fossil fuel emissions. Emissions of $N_2O$ are expected to increase as the world population grows. The gas, $SF_6$, is primarily used as a gaseous dielectric for high-voltage power applications and is emitted where power grids and populations are located. Its emissions are largely due to leakage from power applications, and there is no available substitute compound with similar dielectric properties that is more climate-friendly than $SF_6$.

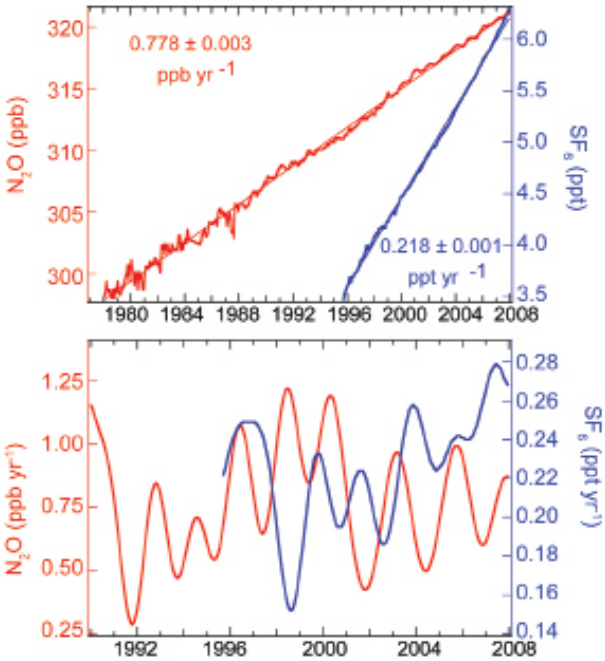


**Fig. 2.20. (top) Atmospheric concentrations for global monthly means vs time for $N_2O$ (in ppb, red) and $SF_6$ (in ppt, blue) with linear regressions as thin lines displayed for the NOAA/ESRL baseline observatories located at Pt. Barrow, AK; Niwot Ridge, CO; Mauna Loa Observatory, HI; American Samoa; and South Pole. Concentrations for $N_2O$ are determined from flask samples during 1977–87 and in situ GCs from 1987 to the present. Atmospheric $SF_6$ concentrations are measured from flask samples during 1996–98 and in situ GCs from 2000 to the present. (bottom) Instantaneous growth rates for the same datasets since 1990.**

### 6) The combined influence of long-lived trace gases on the radiative balance of the atmosphere

Changes in the abundance of long-lived trace gases have a direct and indirect influence on the energy balance of the atmosphere. The direct radiative influence of a trace gas is directly proportional to its atmospheric abundance and how efficiently it absorbs infrared radiation in specific regions of the electromagnetic radiation spectrum (its radiative forcing). High-precision measurements of $CO_2$, $CH_4$, $N_2O$, CFC-12, CFC-11 (the major long-lived greenhouse gases), and 10 minor greenhouse gases obtained from the NOAA global air sampling network were used to calculate the overall change in the direct radiative climate forcing arising from the sum of all of these long-lived gases (Hofmann et al. 2006; Fig. 2.21). This forcing is calculated by considering changes in the abundances of these gases since 1750, which are coarsely derived from ice cores prior to the instrumental record. By mid-2006, the increases in the abundances of all these gases above 1750 levels amounted to an additional direct radiative forcing to the atmosphere totaling approximately 2.66 W $m^{-2}$. Changes in the abundance of $CO_2$ since 1750 accounted for nearly two-thirds of this enhanced radia-

tive forcing (63%).

The NOAA AGGI is based upon the direct radiative forcing calculated from these NOAA measurements (Hofmann et al. 2006). The index is a ratio of direct radiative forcing from all these gases (based upon changes since 1750) relative to the direct radiative forcing calculated from these gases for 1990, the Kyoto Protocol baseline year; indirect effects are not considered in this index. By 2007, the AGGI was 1.242, indicating that the direct radiative forcing arising from increases in the abundance of these trace gases had increased by 24.2% from 1990 to 2007 (Fig. 2.21). Increases in the atmospheric abundance of $CO_2$ accounted for ~80% of the observed increase in the AGGI from 1990 to 2007.

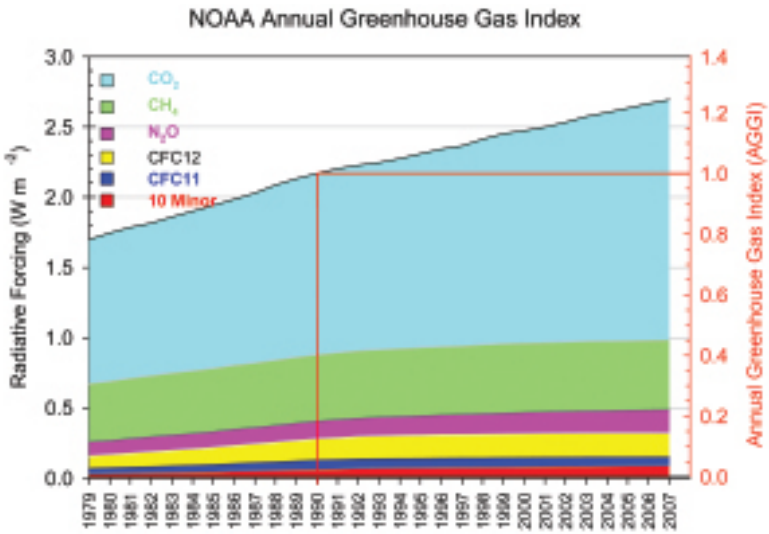


**Fig. 2.21. The direct radiative forcing arising from increases in the abundance of long-lived trace gases in the atmosphere since 1750 and the AGGI (Hofmann et al. 2006). The colored bands indicate the radiative forcing from subsets of gases listed in the caption. Also shown is the NOAA AGGI, which is calculated from the total direct radiative forcing normalized to 1.0 in 1990 (red line), the baseline year of the Kyoto Protocol. [Source: D. Hofmann, NOAA/ESRL.]**

### 7) Global aerosols—A. T. Evan

Aerosols in 2007 were generally in line with recent "climatological" norms. Many of the aerosol anomalies related to smoke from biomass burning observed in 2006 (Evan et al. 2007) did not persist. For example, the 2006 elevated aerosol levels seen at the far northern latitudes or around Indonesia were absent this year. In contrast, smoke from biomass burning over the Amazon basin, an indication of regional deforestation, exhibited levels that were inline with the increasing aerosol trend seen from 2000 through 2005, a stark contrast to the much clearer skies noted in 2006 (Koren et al. 2007).

The analysis of aerosols in this year's report focuses on the examination of satellite AOD retrievals from the MODIS onboard the *Terra* satellite at 550 nm[3] (Remer et al. 2005) and the AVHRR at 670 nm (AVHRR date were obtained through the PATMOS-x project Web site: http://cimms.ssec.wisc.edu/clavr/patmosx.html) (Ignatov and Stowe 2002a, 2002b). Although the coverage for these polar orbiting satellites is nearly global, retrievals are only made for cloud-free conditions and are limited to oceanic regions (for the AVHRR) or are not retrieved over bright reflecting land surfaces (for the MODIS). Additionally, the MODIS and AVHRR products do not measure particle composition, although information about the particle's nature can be inferred from the MODIS aerosol size modes (small or coarse). Despite these limitations, the 7-yr MODIS and 26-yr AVHRR records are reliable indicators of change on inter-annual to multidecadal time scales.

Figure 2.22 is a map of the global mean aerosol optical depth from the MODIS *Terra* satellite, where the global mean AOD is 0.15. The spatial distribution of global AOD in 2007 was similar to recent years. High AOD associated with mineral dust over the tropical Atlantic, West Africa, the Middle East, and the north Indian Ocean dominated much of the aerosol loadings. High aerosol loadings were also concentrated along the northern boundary of the Indian subcontinent and eastern China. These aerosols were likely anthropogenic in nature, as evidenced by higher values of the small mode fraction here (a measure of the fractional composition of the aerosol optical depth by small particles, not shown). The Taklimakan Desert is a major dust source region that resides in western China, upwind of Beijing and the Yellow Sea. Therefore, the AOD values there are a mix of anthropogenic and mineral aerosols (Kaufman et al. 2002). Biomass burning in the Amazon basin along the so-called arc of deforestation dominated

[3] MODIS data used in this paper were obtained through the Giovanni online data system, developed and maintained by the NASA Goddard Earth Sciences (GES) Data and Information Services Center (DISC).

the aerosol signal in South America.

Figure 2.23 is a 1982 to 2007 time series of global, oceanic, AOD retrievals from the AVHRR. This previously reported downward trend in aerosol loadings (Mishchenko et al. 2007), superimposed over spikes in AOD in 1982 and 1991 associated with the eruptions of El Chichón and Mt. Pinatubo, respectively, is likely a reflection of reduction in Saharan/Sahel dust storm activity. It may also, more importantly, reflect reductions in anthropogenic sulfate aerosols by some industrialized nations over the same time period.

Comparison of aerosol optical depths in 2007 with measurements in 2006 indicates three regions with notable variability: the Amazon basin, Indonesia, and the northern boreal forests of Eurasia. In 2006 aerosol loadings in the Amazon were at their lowest point since at least 2000 (Koren et al. 2007), but in 2007 these measurements were the highest on record, at about 1.5 times the 2006 estimations (Fig. 2.24). It is unclear if these low 2006 AOD levels, and the subsequent high 2007 values, are the result of policy shifts or reflect variability in the local meteorology (Koren et al. 2007). For example, cloudiness has a significant effect on the AOD record and may have played some role in these annual values. In addition when low-level winds are predominately easterly in this region, aerosols from the Amazon basin are not easily advected past the Andes and over the South Pacific. Therefore, the long-term AVHRR oceanic record of aerosols is currently of little help in identifying the interannual to decadal variability in aerosols from this region.

In Indonesia, aerosols associated with biomass burning in 2007 were significantly lower than the previous year. In 2006, there was an increase in biomass burning, associated with drier than average conditions. This was associated in part with an El Niño event that developed late in the year (Evan et al. 2007). In 2007, a moderate La Niña event developed in September, and these conditions contributed to higher precipitation totals across Indonesia and a reduction in biomass burning episodes compared to 2006 (van der Werf et al. 2004). When considering the longer AVHRR aerosol record, which includes several positive and negative ENSO events, there were no statistically significant aerosol anomalies in this region for 2007. Last, aerosols associated with the northern boreal forests of Eurasia returned to mean climatological levels in 2007, for both the MODIS and AVHRR data, following the elevated activity associated with biomass burning that was observed in 2006 (Stohl et al. 2006).

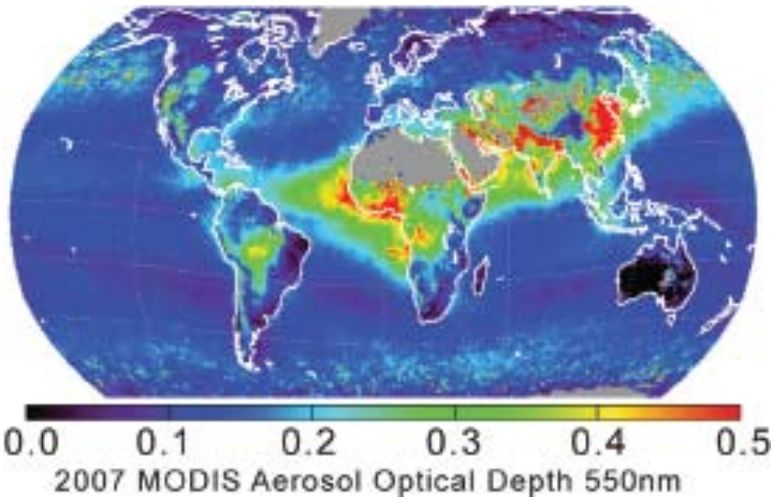


**Fig. 2.22. Global map of mean AOD values at 550 nm from the MODIS *Terra* satellite.**

### e. *Global winds*—S. R. Smith, R. N. Maue, and M. A. Bourassa

Monthly global wind speed and sea level pressure anomalies (Fig. 2.25) with respect to the long-term mean (1968–96) are constructed from the NCEP–NCAR reanalysis (Kalnay et al. 1996). Overall, the global wind speed and sea level pressure anomalies are weaker in the tropics and stronger in the midlatitude and polar regions. With a few exceptions, larger anomalies occur over the oceans.

#### 1) Ocean winds

Wind anomalies were most pronounced over the Southern Ocean throughout 2007. The wind anomaly pattern associated with the building La Niña pattern was present in the tropical Pacific and a stronger summer Indian monsoon pattern occurred. Elsewhere, the anomaly patterns lacked spatial and temporal consistency from month to month.

##### *(i) Southern Ocean*

In a pattern similar to 2006, the atmospheric circulation over the circumpolar Southern Ocean exhibited a series of positive and negative wind speed anomalies for all months, with the possible exception of January and February. A pattern of alternating pressure anomalies in the circumpolar trough (~40° to 60°S) results in stronger pressure gradients, which are associated with the large wind speed

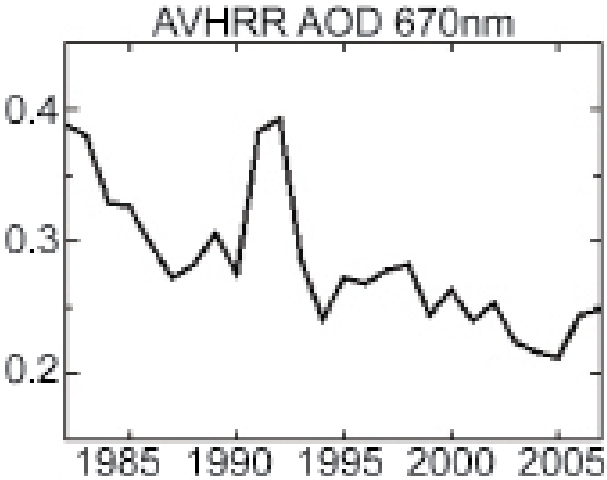


**Fig. 2.23. Time series of global oceanic AOD values at 670 nm from the AVHRR.**

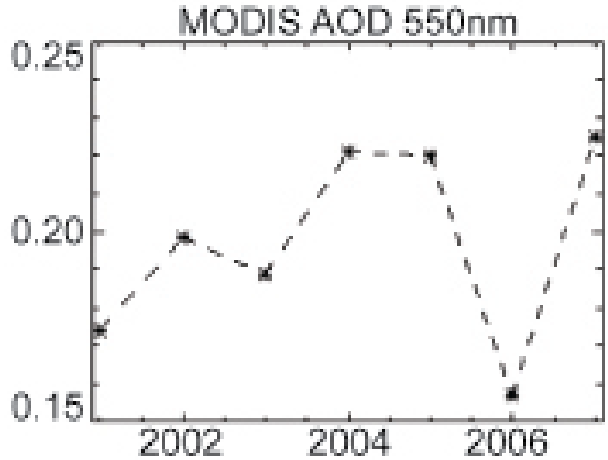


**Fig. 2.24. Time series of annual mean AOD over the Amazon basin from MODIS.**

anomalies. The wind and pressure patterns are indicators of anomalous storm activity in the Southern Ocean. The patterns do not necessarily indicate more or less storms: they could be related to a shift in the location of the storm tracks. However, the long bands of greater wind speeds in March through August suggest an atypically strong surface manifestation of the polar vortex during the austral winter.

*(ii) Tropics*

Starting in June, a pattern of stronger winds appeared in the equatorial Pacific Ocean near the date line. This was the onset of the easterly anomalies associated with La Niña. The easterly anomalies became more prominent in August through December, with a drop in strength in October. The location and monthly variation of the NCEP–NCAR anomalies match well with the monthly Florida State University wind analysis based on ship and mooring observations (available in the Climate Diagnostics Bulletin, www.cpc.ncep.noaa.gov/products/CDB/).

2) Continental winds

Winds over the land surface showed very few notable anomalies during 2007. Although many individual months showed anomalies over the land surface (e.g., stronger winds in Central America in November), these anomalies rarely persisted from month to month. The exceptions occurred around the North Atlantic region over Europe and Greenland.

*(i) Europe*

During January, lower pressure over the Russian Arctic and higher pressure to the southwest resulted in stronger winds over most of northern Europe. A similar pressure pattern existed in March through May, but the impacts on European winds varied from month to month. High pressure anomalies during October and November resulted in weaker winds over northwestern Europe.

*(ii) Greenland*

Positive wind anomalies persisted over Greenland throughout 2007. The wind anomalies peaked in strength during February and July (with anomalies near 4 m $s^{-1}$) and were weakest during September and October. With the exception of February, the wind anomalies were not clearly associated with gradients in the sea level pressure anomalies. This may, in part, be due to the sea level pressures not being a representative measure over the high ice plateau of interior Greenland. The reduction of surface pressures to sea level is problematic over very high terrain.

*f. Major modes of Northern Hemisphere variability: The Arctic Oscillation and the Pacific–North American pattern*—M. L. L'Heureux, J. C. Gottschalck, and M. S. Halpert

The two leading patterns of Northern Hemisphere climate variability are the AO and the PNA pattern. These patterns collectively explain nearly one-third of the month-to-month variations in SLP, and nearly half of the variance in the wintertime mean SLP (Quadrelli and Wallace 2004). The AO, which is the first leading mode, features a "zonally symmetric" pattern featuring anomalous atmospheric pressure in the polar region and opposite-signed anomalies focused over the northern Pacific and Atlantic Oceans (Thompson and Wallace 2000). In contrast,

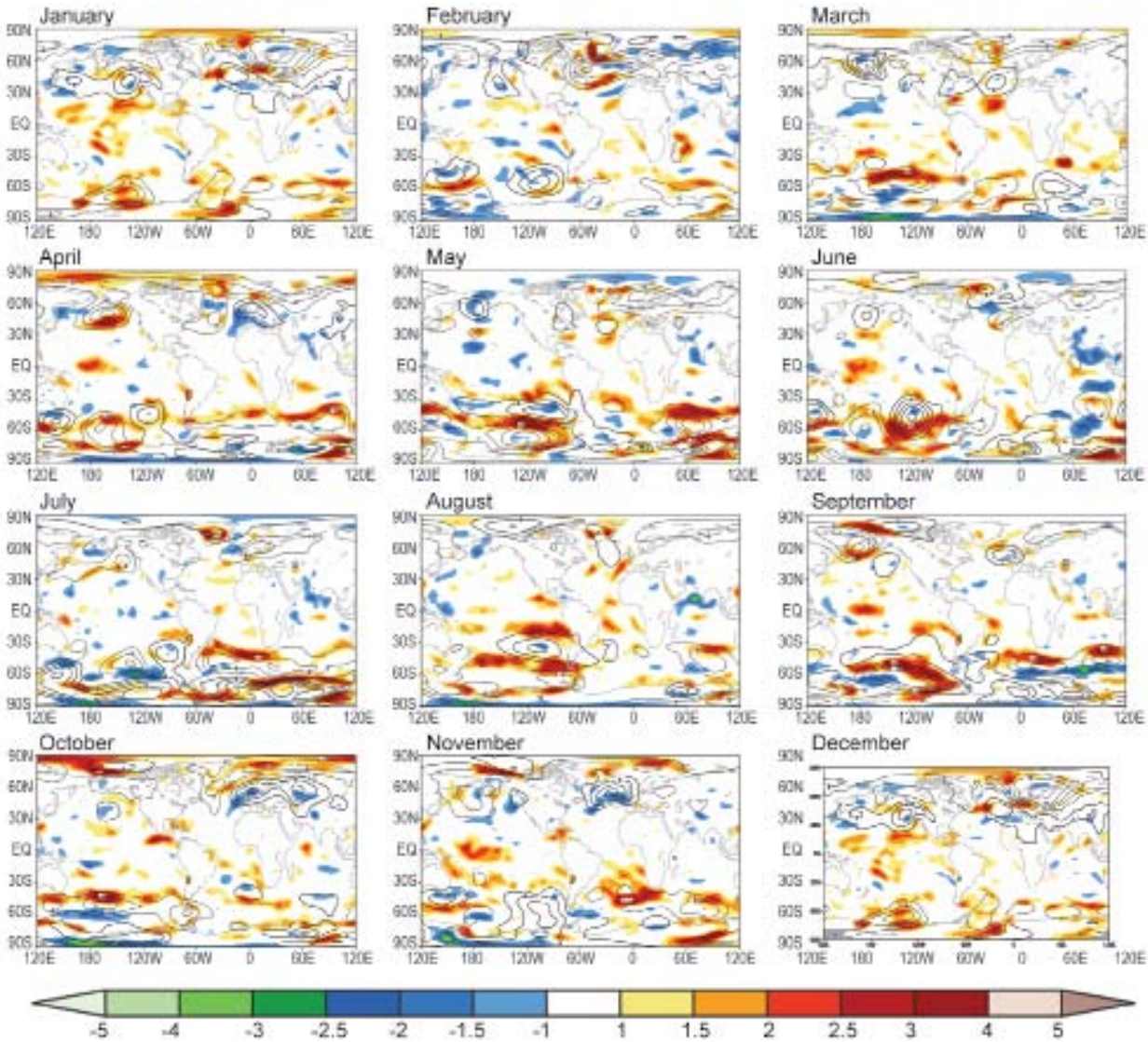


**Fig. 2.25. Wind speed (m s$^{-1}$) and sea level pressure (hPa) anomalies during each month of 2007. Sea level pressure contoured every 3 hPa with negative anomalies dashed.**

the PNA is the second-leading mode and is considered a "zonally asymmetric" pattern with alternating centers of anomalous pressure that arc northeastward through the North Pacific Ocean and then curve southeastward into North America (Wallace and Gutzler 1981).

### 1) Record PNA pattern during July–September

The positive phase of the wintertime PNA at 500 hPa is typically characterized by a "wave train" of above-average heights in the vicinity of Hawaii and over western Canada, and below-average heights over the North Pacific and southeastern United States The positive polarity of the PNA is often cited to describe the midlatitude response to El Niño, which implies the PNA can be externally forced (e.g., tropical SSTs), but other research has indicated that the PNA pattern is a distinct natural mode of climate variability arising from internal atmospheric dynamics (Simmons et al. 1983; Mo and Livezey 1986; Straus and Shukla 2002).

The PNA is calculated using a rotated empirical orthogonal function procedure and has its strongest amplitude during the winter season. The PNA has a signal throughout the year, with the wave train varying in location and strength depending on the season. In particular, the wave train is weaker and shifts poleward during the summer months JAS (Fig. 2.26a), with weaker centers of action arcing through the Pacific Ocean and stronger centers of action arcing

through the western Arctic Circle toward the Hudson Bay. However, even when considering the muted PNA pattern, the JAS 2007 PNA featured an unusually strong signal in the observed circulation anomalies, and may have helped to modify the Pacific storm track during the period.

During JAS 2007, the positive polarity of the PNA pattern projected very strongly onto the observed 500-hPa height pattern (Fig. 2.26b). Anomalous ridging was observed at lower latitudes in the North Pacific Ocean and more notably just north of Alaska. Weak anomalous troughs were observed just to the west of the Aleutian Islands and near Hudson Bay over northern Canada. Accordingly, the PNA index for JAS 2007 was three standard deviations above the 1950–2007 JAS mean, constituting a 1 in 333 yr chance of occurrence (Fig. 2.26c) and is the largest departure recorded in the historical record.

The observed upper-level circulation over the Pacific was conducive to a stronger jet stream and downstream divergence in the jet exit region, which helped to enhance storminess across a wide swath of the central and eastern North Pacific Ocean. During JAS 2007, at least a 25% increase in those storms was observed across a west–east trajectory in the central North Pacific with a nearly 300% increase observed in the eastern North Pacific.

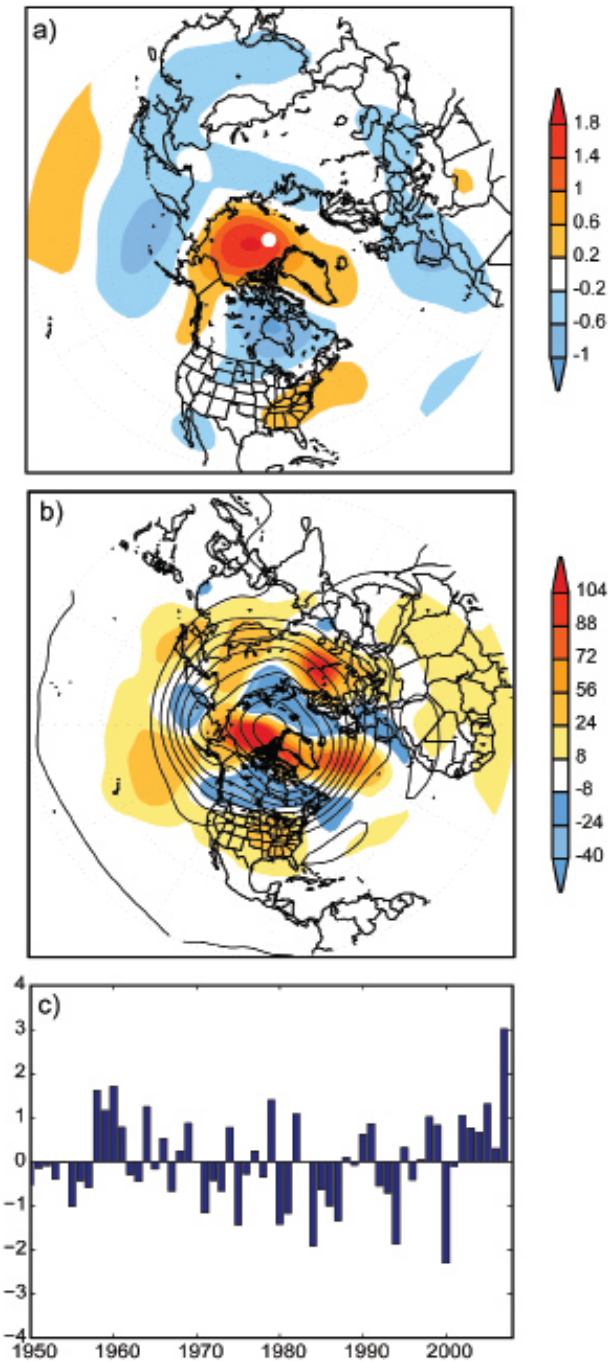


**Fig. 2.26. (a) Jul–Sep PNA loading pattern (dimensionless) based on a rotated empirical orthogonal function calculation using 500-hPa geopotential height anomalies. (b) Mean 500-hPa height (contours, contour interval 50 m) and height anomalies (shading, units are in m) for Jul–Sep 2007. (c) Jul–Sep seasonally averaged PNA index values standardized based on all Jul–Sep values from 1950 to 2007.**

### 2) The AO flips sign during the 2006–07 winter

The AO, or the NAM, is the leading mode of variability in the Northern Hemisphere and is characterized by north–south shifts of circumpolar westerly flow in the Northern Hemisphere. The high index polarity is defined by a poleward shift of the westerly midlatitude jet, while the low index polarity occurs when the jet is equatorward of its average position (Thompson and Wallace 1998, 2000). While distinguished by a hemispheric-wide pattern, the AO has its greatest teleconnection in the Atlantic basin, where it is highly correlated with the regional NAO pattern (Thompson et al. 2003). The AO, however, describes more of the hemispheric trends and interannual variability of temperature, with the high index phase associated with less frequent cold air outbreaks into the midlatitudes and more cold air outbreaks for the low index phase (Thompson and Wallace 2001).

The mean 500-hPa circulation pattern during DJF 2006–07 was characterized by a large degree of zonal symmetry that projected strongly onto the AO. The pattern featured the positive phase of the AO from December 2006 to mid-January 2007 and the negative phase from mid-January through the end of February 2007 (Fig. 2.27). Correspondingly, anomalous temperatures also had a hemispheric-wide signal, with anomalies of like sign observed over the midlatitudes in North America and Eurasia during both halves of the

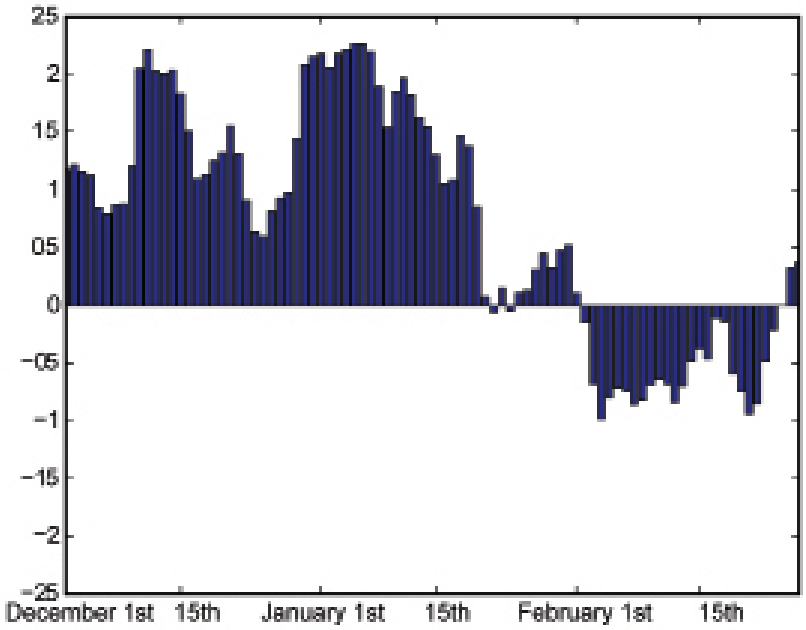


**Fig. 2.27. Standardized time series of the AO index for daily values between 1 Dec 2006 and 28 Feb 2007.**

winter.

Consistent with the positive phase of the AO, the 500-hPa geopotential heights during 1 December 2006–15 January 2007 featured negative anomalies throughout the polar latitudes stretching from Greenland toward Alaska, and positive anomalies throughout the midlatitudes (Fig. 2.28a). During this period, the midlatitude jet streams were displaced poleward and high-latitude blocking was minimal, which limited cold air outbreaks into the middle latitudes. Consequently, this pattern was linked to above-average surface temperatures across much of Eurasia, Canada, and the central and eastern United States (Fig. 2.28b).

In contrast, during the latter half of the winter season (15 January–28 February 2007), the 500-hPa circulation shifted with positive height anomalies prevailing over the Arctic Circle and negative height anomalies over northern Eurasia and from the north-central/eastern United States eastward through the Atlantic Ocean (Fig. 2.28c). This pattern was associated with increased high-latitude blocking, and numerous cold air outbreaks into both North America and the northern half of Eurasia. These conditions were consistent with the negative polarity of the AO and led to an abrupt end to the exceptionally mild winter conditions seen in these regions during December and early January, with below-average temperatures dominating these regions during the second half of the winter (Fig. 2.28d).

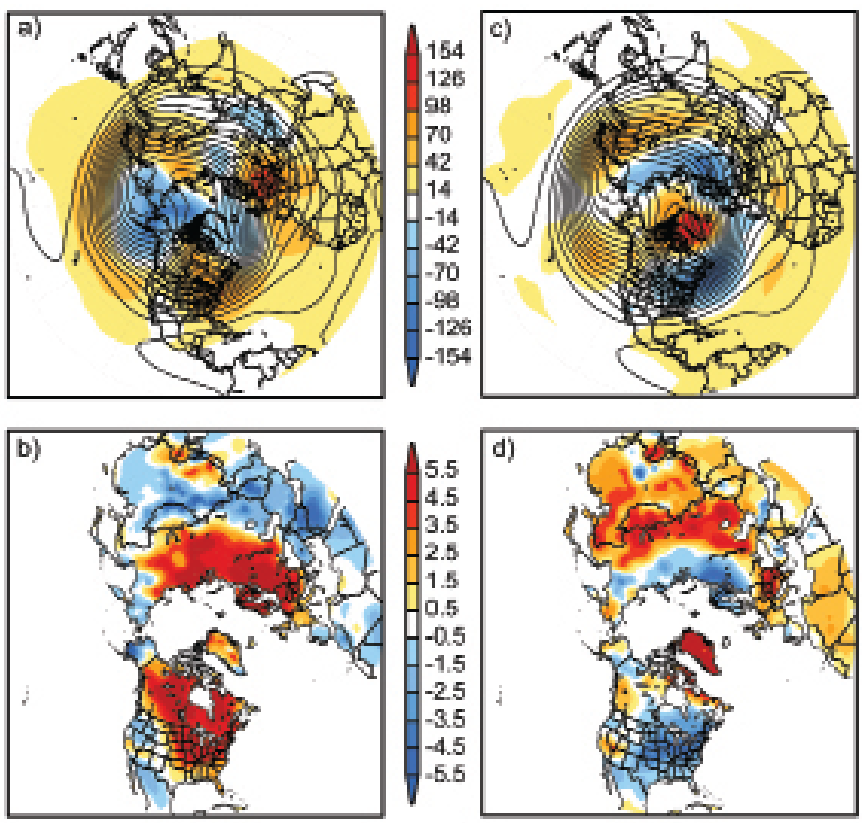


**Fig. 2.28. (a) Mean 500-hPa height (contours, contour interval 50 m) and height anomalies (shading, units are in m) for 1 Dec 2006–15 Jan 2007. (b) Surface temperature anomalies based on CDAS (Kalnay et al. 1996) for 1 Dec 2006–15 Jan 2007 (climatology calculated using the first four harmonics during 1979–95). (c) Same as (a) except for 15 Jan–28 Feb 2007. (d) Same as (b) except for 15 Jan–28 Feb 2007.**